



Development of a photoacoustic monitoring system for the study of laser ablation processes upon the removal of encrustation from stonework

Athanasia Papanikolaou

*Thesis submitted in fulfillment of the requirements for the degree of Master of Science
in the Faculty of Physics*

Scientific Committee

Prof. D. Charalampidis
(supervisor)

Prof. D. Anglos

Dr. I. Zacharakis

**Research
Advisors**

Dr. P. Pouli

Dr. G.J.
Tserevelakis

Heraklion, September 2018

Contents

Contents	3
Acknowledgments.....	5
Περίληψη	6
Abstract.....	7
Introduction.....	8
On line monitoring of laser cleaning	8
PA effect for the evaluation of laser cleaning processes previous studies	9
Laser cleaning of dark crusts from stone: The Dual wavelength methodology ...	10
Theory	12
Ablation mechanisms	12
Photothermal ablation.....	12
Photochemical ablation.....	13
Photomechanical ablation.....	14
The Photoacoustic effect	14
Derivation of the Photoacoustic equation.....	15
Thermal and stress confinement conditions	16
Photoacoustic pressure rise.....	18
Non Linear PA generation.....	19
Materials and Methods.....	20
Experimental Equipment.....	20
Laser System and Parameters	20
Experimental Setup.....	20
Hybrid Photoacoustic and Optical System	21
Recording protocol	23
Experimental Techniques.....	23
SEM.....	23
Profilometer	24
UV-VIS spectrophotometer	25
Samples	25
Marble Samples Description.....	25

Sample Preparation	26
Results.....	27
Ablation and Extraction Thresholds.....	27
Marble Ablation Thresholds	27
Artificial Crust Extraction Thresholds	29
Non Linear PA effect - Ablation coefficients	31
Comparison of the generated PA signal for marble and carbon	34
Estimation of the local Temperature rise	37
PA signal and Laser Induced Ablation Mechanisms: Comparison between 1064 and 355nm.....	38
Real time Photoacoustic and Optical Monitoring of laser cleaning.....	42
Cross Correlation photoacoustic signal analysis	48
Implementation of Cross Correlation for the Monitoring of laser cleaning	48
Evaluation of ablation thresholds with Cross Correlation analysis	58
Conclusions and Future Research	62
References.....	63

Acknowledgments

I would like to thank some people who contributed to the successful completion of this Master Thesis. First of all, I would like to express my highest appreciation to my advisor Dr. Paraskevi Pouli for her guidance, encouragement and support, during the development of my thesis. Her feedback and advices were more than valuable for me and were leading my efforts.

Furthermore, I would like especially to express my gratitude to Dr. George J. Tserevelakis, who had the original idea for this project, for his constant support and guidance. His scientific expertise helped in the in depth understanding of the phenomena and stages of the experimental process, while his great experience played a decisive role in the rapid solution of any encountered problems.

Special thanks to Prof. Dimitrios Charalambidis (Professor, Physics Department, University of Crete), Prof. Demetrios Anglos (Professor, Department of Chemistry, and University of Crete) and Dr. Giannis Zacharakis (Research Scientist, In vivo Optical Imaging group, IESL FORTH) that accepted to be members of my evaluation committee for my Master Thesis.

Finally, I could not exclude from my acknowledgments Ms Kristalia Melessanaki for her constant support and encouragement, as well as, the people of the Photonics for Cultural Heritage Group for our excellent cooperation.

Περίληψη

Στο πλαίσιο της παρούσας διπλωματικής εργασίας, αναπτύχθηκε ένα πρωτότυπο υβριδικό φωτοακουστικό και οπτικό σύστημα για την παρακολούθηση, σε πραγματικό χρόνο, εφαρμογών καθαρισμού με λέιζερ. Αυτή η διάταξη επέτρεψε την καταγραφή των ακουστικών κυμάτων που δημιουργούνται κατά τη διαδικασία της φωτοαποδόμησης στην περιοχή των MHz. Η καταγραφή του παραγόμενου φωτοακουστικού σήματος, σε συνδυασμό με οπτικές εικόνες υψηλής ανάλυσης, παρέχει την δυνατότητα της επιτόπιας παρακολούθησης του καθαρισμού με ακρίβεια. Για το σκοπό αυτό χρησιμοποιήθηκαν τεχνικά δείγματα, που αποτελούνται από μαρμάρο και προσομοίωση περιβαλλοντικών επικαθίσεων, στα οποία έγιναν δοκιμές καθαρισμού με λέιζερ. Η ακτινοβολήση πραγματοποιήθηκε με δυο δέσμες λέιζερ, μια υπέρυθρη (1064 nm) και μια υπεριώδη (355 nm), οι οποίες χρησιμοποιήθηκαν μεμονωμένα ή/και ταυτόχρονα, ενώ η παρακολούθηση της διαδικασίας ήταν δυνατή μέσω της καταγραφής και της επεξεργασίας των παραγόμενων φωτοακουστικών σημάτων. Συγκεκριμένα, η χρήση αυτού του υβριδικού συστήματος επέτρεψε τον ακριβή προσδιορισμό του αριθμού των παλμών λέιζερ που απαιτούνται για την πλήρη απομάκρυνση της ανεπιθύμητης κρούστας επικαθίσεων κατά την ακτινοβολήση και συνέβαλε στην διερεύνηση των εμπλεκόμενων μηχανισμών φωτοαποδόμησης.

Για το σκοπό αυτό η μεταβολή του παραγόμενου ΦΑ σήματος μελετήθηκε συνδυαστικά με την εξέλιξη της διαδικασίας του καθαρισμού, όπως αυτή αποτυπώνεται στην ακτινοβολημένη επιφάνεια, η οποία αξιολογήθηκε με μια σειρά από αναλυτικές τεχνικές (προφίλομετρία, ηλεκτρονικό μικροσκόπιο σάρωσης και φασματοφωτόμετρο). Επιπλέον, μέσω της μελέτης του παραγόμενου φωτοακουστικού σήματος ήταν δυνατόν να υπολογιστεί η αναλογία της σχετικής αύξησης της θερμοκρασίας (T_{IR} / T_{UV}) που αναπτύσσεται στο υλικό λόγω της αλληλεπίδρασης του με τη δέσμη του λέιζερ και να συνδεθεί με τους εμπλεκόμενους μηχανισμούς αποδόμησης.

Τα αποτελέσματα από την μελέτη αυτή αποδεικνύουν την δυνατότητα της συνδυασμένης φωτοακουστικής και οπτικής προσέγγισης όσον αφορά την επιτυχή παρακολούθηση του καθαρισμού με λέιζερ καθώς και την μελέτη των κυρίαρχων μηχανισμών φωτοαποδόμησης για κάθε μήκος κύματος. Στην κατεύθυνση αυτή, η παρούσα εργασία συνεισφέρει στην εξήγηση της μεθοδολογίας καθαρισμού η οποία συνδυάζει 2 δέσμες λέιζερ που έχει αναπτυχθεί τα τελευταία χρόνια και στοχεύει στη μείωση φαινομένων δυσχρωματισμού που παρατηρούνται στις ακτινοβολημένες επιφάνειες από τις οποίες έχουν αφαιρεθεί περιβαλλοντικές επικαθίσεις.

Abstract

Laser cleaning of environmental encrustation from outdoor monuments and sculptures is a well - established technique successfully applied in the preservation of Cultural Heritage. Conservators commonly rely on their experience and visual assessment in order to set the limits for the termination of the laser cleaning process. However, this practice can jeopardize the cleaning outcome as micro-damage may occur. In this respect, the accurate and real time monitoring of laser cleaning interventions remains an open issue urging for further investigation, particularly when employing cleaning methodologies involving objects and deposition layers that present similar ablation threshold values. Thus the cleaning process becomes more demanding and the decision as regards the precise number of pulse that removes the unwanted layer gets important.

In the context of this thesis, a prototype hybrid photoacoustic (PA) and optical system for the on-line monitoring of pulsed laser cleaning procedures was developed. This approach has enabled the “listening” of the sound produced during the ablation through the recording of acoustic waves in the MHz regime. The intrinsically generated PA signals combined with high resolution optical images provide the opportunity to follow the cleaning process accurately and in real time. Technical simulation samples have been used to demonstrate the potential of this novel technique, while the real time monitoring of the cleaning process has been successfully implemented, for the individual use of IR and UV wavelengths, as well as, their simultaneous use in various energy fluence ratios. This state of the art approach has allowed the precise determination of the critical number of laser pulses that eliminate the encrustation layer, and most importantly enables the understanding of the involved ablation mechanisms.

Specifically, variations at the amplitude of the PA signal have been used as an indicator of the different laser ablation processes and, by means of cross correlation analysis, they enabled the detection of changes to the irradiated surfaces. The final irradiated surface was also examined with analytical techniques (SEM, profilometry and reflectance measurements) aiming to evaluate and assess the cleaning result. In addition, through the study of the generated PA signal it was possible to calculate the relative temperature ratio rise (T_{IR}/T_{UV}), induced on the material during the laser ablation and thus associate it with the involved mechanisms.

The results from the above study will be presented with the aim to demonstrate the successful monitoring for the unwanted material removal, as well as, to explain the dominant ablation mechanisms for each wavelength upon the laser cleaning of encrustation from stonework and thus to discuss the role of the two-wavelength laser cleaning methodology to avoid discoloration phenomena.

Introduction

Laser cleaning of artworks has been established as a common conservation intervention in the last decades, often substituting conventional cleaning methods, due to its unique properties. It was first investigated by Asmus in the early 70s and since then, a significant amount of research efforts have been dedicated to the field of Cultural Heritage (CH), with a wide range of conservation applications [1-4]. Lasers offer a number of advantages such as selective and gradual material removal, high precision and control during the cleaning, while they are environmentally safe compared to conventional cleaning methods based on chemicals. Laser cleaning relies on the selective ablation of the unwanted deposits due to their intense absorption of pulsed laser irradiation. It is a delicate and irreversible process which requires careful selection of irradiation parameters and thorough knowledge of the involved ablation mechanisms, given that the nature of the deposition layers is exceptionally complex, and the condition of the original surface is fragile [5, 6]. For example, overexposure to laser pulses can result in damage of the substrate; on the contrary, if the pulse number is less than required for the total elimination of the crust, the final surface may have residues and be discolored. In the case where the cleaning is performed with an automated scanning system, attention must be given to the regulation of the number of pulses upon the local thickness and irregularities of the crust. For this reason, research efforts have been dedicated to the optimization of the cleaning outcome along with the real time monitoring of the cleaning progress through micro and/or non-destructive analytical and diagnostic techniques.

On line monitoring of laser cleaning

The real time monitoring of the cleaning progress has been considered through a variety of analytical techniques, most of the times with encouraging results; however there are also certain limitations depending on the specific cleaning case such as the sensitivity of the investigated technique, its resolution and its cost. Laser induced breakdown spectroscopy (LIBS) [2, 7-10], Multispectral and Hyperspectral imaging [11, 12] and Digital Holographic speckle interferometry [13] are among the analytical techniques which has been considered for the real time monitoring of laser cleaning in a variety of applications such as the removal of environmental crust from stone, cleaning of wall paintings, elimination of aged varnish from wood and paintings.

The use of LIBS as a monitoring tool has been investigated on the basis of the collection and subsequent analysis of the ablation plume generated during the cleaning process. In the case that a significant difference is observed between the LIBS spectra of the unwanted layer and the original surface, it is possible to control the process of cleaning using custom made signal processing algorithms [2, 8, 10]. However, in order to obtain a LIBS spectra, high fluence values are required in most of the times, usually well-above the ones commonly used for cleaning interventions (e.g. in the cleaning of black crusts from stone), limiting thus the capabilities of the technique. Another approach is the possibility of using two distinct laser pulses [9];

one for the cleaning of the object and a second for the acquisition of LIBS spectra. Nevertheless, as LIBS is a micro-destructive technique this is an important drawback for its wide implementation as a monitoring tool.

A non-contact technique which has also been involved for the on-line monitoring of laser cleaning interventions is the multispectral imaging. Multispectral imaging systems have been successfully used to assess the laser cleaning progress following every single laser pulse. This methodology has been successfully tested for cleaning cases of encrusted stonework. Multispectral imaging exploits the possibilities offered by the differential penetration of monochromatic light in matter, enabling the real-time mapping of the depth of cleaning based on the calculated differences of images obtained at two different spectral bands. Still the employment of MSI as a monitoring technique presents certain limitations, as it requires extensive studies dedicated on the specific object to be cleaned and is also significantly depended on the ambient light conditions [11, 12].

PA effect for the evaluation of laser cleaning processes previous studies

Another approach that has also been adopted for the real time and in situ monitoring of laser cleaning applications is the photoacoustic (PA) technique. The photoacoustic effect has found many applications in various fields of research, mainly focused on biomedical imaging [14, 15] and analysis of several materials, as an alternative to traditional absorption spectroscopy[16]. Nevertheless, PA techniques have also been developed for the monitoring of laser cleaning interventions in works of art. A number of research efforts have been made involving either the use of conventional microphones or ultrasonic transducers with central frequencies in the MHz regime, aiming to detect the incident laser pulse that eliminates the encrustation layer. The gradual material removal can be monitored through variations of the PA amplitude, attributed mainly to the different inherent absorption properties of the over - layer and the underlying material.

Leung and Tam [17] in 1992 were the first to use pulsed laser induced PA signal detection as a monitoring technique for ablation processes. The authors studied and monitored the PA signal generated, in the regime of 1 MHz, due to irradiation of polyimide and Si wafer samples by means of a KrF excimer laser, at fluence values below and above the ablation thresholds. Copper et al. [3], used acoustic monitoring to investigate the selective removal of black crusts from polluted limestone. They demonstrated that the amplitude of the generated PA signal can be used as a measure of material removal and confirmed the advantages of the wet cleaning, using a Q-Switched Nd:YAG laser at 1064nm and a dynamic coil microphone with a frequency response between 100Hz and 12kHz.

Later, Bregar et al [18], used a multiple-pass laser beam deflection probe technique/method [19] for the detection of the PA signal in the regime of 10MHz implementing a XeCl laser at 308nm. Using this methodology they monitored on line the cleaning progress for paint removal from stainless steel, glass and marble.

Similarly, Jankowska et al. [20] examined the acoustic effect for the monitoring of black crust removal from sandstone. They used a Q-Switched Nd:YAG laser at 1064 and 532 nm in a broad range of laser fluence values, for samples covered with environmental crust, as well as, artificial ones. In their study they associated the exponential signal decay with the decreasing crust thickness. Determination of the ablation thresholds of different graffiti sprays was performed by Gómez et al [21], using a PA technique. Specifically, they investigated the ablation thresholds of commercial silver, white, black gold and pink graffiti sprays deposited on glass slabs using wavelengths of 1064 nm and 308 nm. In another relevant study, Villareal-Villela et al. [22] introduced the Fast Fourier Transform of the acquired signal in the context of a Photoacoustic Induced by Laser Ablation (PILA) technique for the monitoring of laser assisted paint removal from metallic surfaces. They studied the amplitude of the signal and the magnitude of the FFT for the evaluation of the cleaning progress using a passively Q-Switched Cr:YAG laser at 1064nm. Finally in a recent research, Tserevelakis et al. [23] employed the PA technique for the monitoring of laser cleaning of commercial black graffiti from marble. They used a Q-switched Nd:YAG laser at 1064 nm and a piezoelectric transducer at 5 MHz to investigate the outcome of different irradiation conditions in varying fluence values. They introduced for the first time the predictive potential of the PA technique, by developing a statistical methodology for the accurate detection of onsets regarding the paint ablation, efficient cleaning and damage induced to the marble during the laser cleaning process.

Laser cleaning of dark crusts from stone: The Dual wavelength methodology

One of the most common applications of laser cleaning, which will also be investigated in the context of this thesis, is the removal of dark colored pollution crusts from stone substrates. Those crusts are often developed on the surface of monuments exposed to urban environment due to the microclimate, acid rain, humidity and airborne particles [24]. In an effort to remove the crust from the surface of the marble, while respecting protective layers such as patinas, IR lasers were used; however, yellowing of the irradiated surfaces appeared as an undesirable side effect. The yellowing or discoloration effect has been extensively studied and a number of hypothesis regarding its origin have been developed through the last years [25-27]. In brief, the main prevailing hypothesis upon yellowing are: a) the revealing of pre-existing layers either intentionally applied or naturally developed on the stone, b) the staining of the original stone surface due to migration of water soluble organic compounds from the crust towards the underlying stone[28, 29], c) the chemical transformation of iron oxides such as Fe_2O_3 , into magnetite (Fe_3O_4), and d) the selective vaporization of black components from the crust layer which leads to differential scattering of the light [30], under moderate laser ablation conditions.

With the aim to overcome the challenge of laser induced yellowing, a laser cleaning methodology has been developed[6, 31], in which two wavelengths from the same laser system are used simultaneously to effectively remove the encrustation from the

marble's surface without changes to its color, chemistry or structure. The effectiveness of this methodology relies on the blending of an IR and an UV beam, at a specific ratio and fluence values which provides the opportunity to efficiently remove the encrustation layer. In the simultaneous combination, each wavelength induces different ablation mechanisms: the IR wavelength is responsible predominantly for photothermal phenomena while the UV mostly for photochemical. On the basis of the different absorption properties of the involved materials to the applied laser wavelength, the removal processes vary significantly in each case. One hypothesis is that upon UV irradiation, organic components and gypsum are preferentially removed, while upon IR irradiation Fe-rich particulates are effectively ablated. Therefore, the simultaneous combination of the two beams removes dark colored particles and organic compounds along with gypsum from the crust at the same time, resulting thus into a homogeneous and efficient cleaning procedure[27].

In this direction, we have developed a prototype hybrid photoacoustic (PA) and optical system for the on-line monitoring of pulsed laser cleaning interventions. To demonstrate the capabilities of this approach, a common laser cleaning case has been selected; namely, the removal of environmental encrustation from stonework. As already mentioned, black crusts are efficiently eliminated through the simultaneous use of two irradiation wavelengths both in IR and UV spectral regimes. The developed setup has been used for the monitoring of cleaning tests performed on simplified simulation samples of marble with environmental encrustation, and highlighted important information regarding the laser induced ablation mechanisms. Prior to any irradiation experiment, the ablation threshold of the marble and the extraction threshold of the simulation crust at 1064 and 355nm were determined.

Theory

Ablation mechanisms

The interaction of a pulsed laser beam with a material can occur through a number of different mechanisms, which are closely dependent to the physicochemical properties of the material as well as various laser parameters such as its pulse duration, wavelength and incident power density. Following light absorption and material excitation, the absorbed energy can induce a number of processes which can be categorized as photothermal, photochemical, and photomechanical. These ablation mechanisms can be used to describe the effective material removal, as well as, the nature of side effects induced to the objects due to their excess exposure to the laser radiation (i.e. melting, crack formation, discoloration, grain extraction etc.). The precise description of the induced mechanisms, in complex systems such as artworks, is still an open issue for the scientific community; nevertheless, simple phenomenological models describing the phenomena occurring during the ablation on known materials have been developed and can be applied also in the CH field. Most of those models are based on the interaction of the laser beam with organic materials. In the context of this thesis, the ablation mechanisms will be described based on the wavelength of the incident radiation.

Photothermal ablation

Photothermal mechanisms prevail upon nanosecond IR laser ablation, since most of the absorbed energy is converted into heat. The photon energy in this regime (i.e. at 1064nm is 1.2 eV) is less than the energy required to break most covalent chemical bonds in the molecules (by undergoing an electronic transition)[4, 32]. Still the energy is enough to be absorbed into the vibrational modes of the molecule directly or indirectly via a low-lying electronic state, resulting into heating of the material. With the condition that enough photons are absorbed, the molecule gets thermally decomposed and subsequently ablation occurs. The ablation of the material occurs due to the conversion of the absorbed energy into heat, which is feasible due to collisions among excited electrons with the lattice of the material, other electrons, impurities or defects of the sample. The laser is assumed to act as an instant heat source, because the time among collisions (10^{-14} - 10^{-12} s) is longer than the pulse duration.

An estimation of the temperature rise during the ablation process is feasible [1, 4, 33] starting from the one dimensional heat conduction equation:

$$\frac{\partial^2 T(z, t)}{\partial z^2} - \frac{1}{k} \frac{\partial T}{\partial t} = 0$$

The addition of a term that describes the heat produced/supplied in the solid at rate A, the previous equation modifies to:

$$\frac{\partial^2 T(z,t)}{\partial z^2} - \frac{1}{D} \frac{\partial T}{\partial t} = \frac{-A(z,t)}{K} \quad (2)$$

where $T(z,t)$ is the temperature distribution, $A(z,t)$ is the heat production per unit volume per unit time, K ($\text{Wm}^{-1}\text{K}^{-1}$) is the thermal conductivity and D (m^2/s) the thermal diffusivity of the material. The thermal diffusivity can also be expressed as $D = \frac{K}{C_p \rho}$, where ρ (kg/m^3) stands for density and C_p ($\text{J}/(\text{kg K})$) for the specific heat capacity.

The above equation can be solved for a semi-infinite slab, under the conditions that:

- There is no phase change in the material
- The material properties are not temperature dependent
- The material absorbs the equal amount of energy throughout the irradiated area
- The beam diameter is larger than the thermal diffusion length
- There is no loss of energy due to re – radiation processes

The solution of equation (2) is[34]:

$$T(z, t) = \frac{2 a I}{K} \sqrt{\frac{Dt}{\pi}} \text{ierfc} \left(\frac{z}{2\sqrt{kt}} \right)$$

where *ierfc* is the integral of the complimentary error function, t is the pulse duration, while α is the absorption of the material at the irradiation wavelength and I is the power density of the laser beam ($\frac{\text{pulse energy}}{\text{pulse length} * \text{beam size}} = \frac{W}{\text{m}^2}$). Therefore at the surface of the sample where $z=0$ the temperature rise is equal to:

$$T(t) = \frac{2 a I}{K} \sqrt{\frac{Dt}{\pi}}$$

The above equation is valid for the pulse duration, while the generated heat is propagating into the material at a distance $d_{th}=2(k t)^{1/2}$. Typical values of d_{th} range from 0.6 until $6\mu\text{m}$, for pulse durations from 10ns up to 10 μs according to Salimbeni in[35]. Once the interaction of the beam with the material stops the temperature falls and heat is conducted in the bulk. The heat propagates in the bulk at a depth described as thermal diffusion length $l_{th}=2(k \tau)^{1/2}$, while the time required for the material to reach into thermal equilibrium is known as thermal diffusion time $\tau_{th}=(k \alpha_{eff}^2)^{-1}$ where α_{eff} is the effective absorption coefficient. This time ranges from microseconds up to milliseconds and when $t \ll \tau_{th}$ the process can be described as thermally confined[2].

Photochemical ablation

In the case of irradiation with UV wavelengths (i.e. 355 nm corresponding to a photon energy of 3.5 eV) photochemical ablation processes become dominant especially for organic materials [2, 4, 32]. The molecules absorb the energy from the

incident laser pulse and electronic transitions to higher states are possible to arise. This can lead to several processes such as heat conduction to the sample without any decomposition of molecules, or also to processes such as bond decompositions. Additional species may be formed by thermal or stress induced breaking of chemical bonds which may also form different kinds of by-products. The products have a larger specific volume than the original material leading to its extraction through explosive ablation with minimal thermal load to the substrate.

Photomechanical ablation

The interaction of pulsed laser beam with a material can result in the formation of stress waves propagating within the sample [2, 4, 36]. The stress waves can derive from a variety of sources such as the temperature rise (thermoelastic stress wave) or the expansion of gas products from photochemical decompositions. Therefore, it can be the result of either one of the ablation mechanisms described earlier. The amplitude of those waves can be several hundreds of bars and if the tensile strength limit of the substrate is exceeded then material is removed via fracture.

The Photoacoustic effect

The photoacoustic effect is the formation of acoustic waves followed by the absorption of light by a material and was firstly discovered by Alexander Graham Bell back in the 1880's. When intensity-modulated (e.g. pulsed light) is absorbed by a material, an acoustic signal is created by the heat flow which leads to pressure fluctuations in the sample.

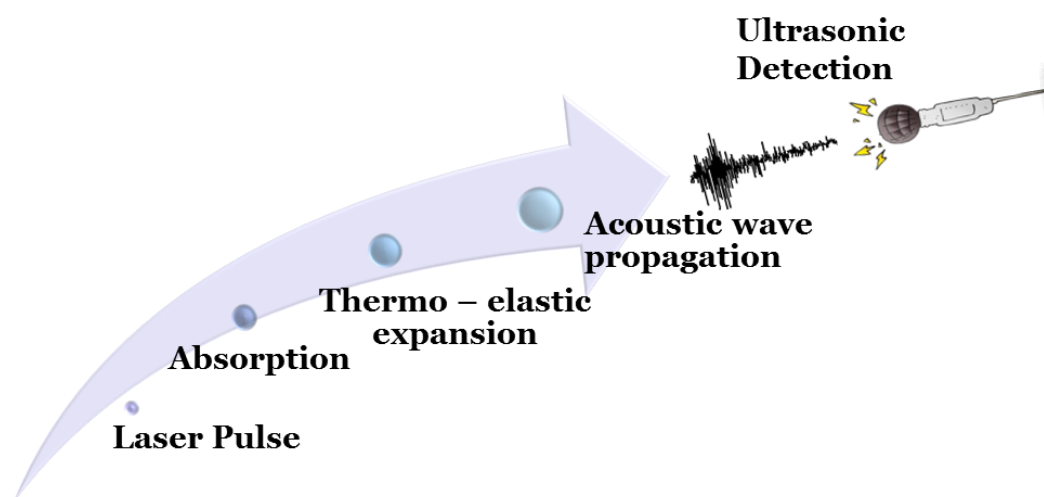


Figure 1: Schematic representation of PA effect

More specifically, initially the absorbed light (for example emitted by a pulsed laser) is converted into thermal energy through non-radiative de-excitation processes, resulting into a rise of the local temperature of the interacting medium. This temperature change is followed by a rapid thermoelastic expansion of the medium, leading to the generation of an initial pressure which propagates in space in the form of acoustic waves. Appropriate detectors (i.e. microphones or piezoelectric sensors) can be used for the recording of the PA waves and the quantification of the

measurements. A typical Photoacoustic signal as measured by an oscilloscope is presented in the following figure¹:

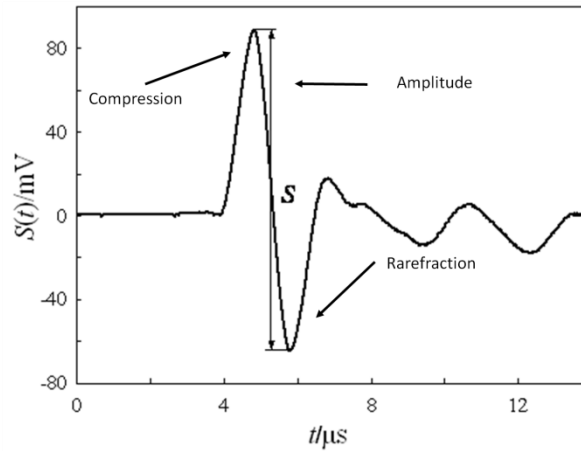


Figure 2: Typical PA signal

The peak to peak amplitude of the signal (S) is defined as the difference between its maximum and minimum value. A typical PA signal, consists of alternating compressions and rarefactions (corresponding to regions of high and low pressure), which are perceived as consecutive peaks and valleys as seen in figure 2. The magnitude of this effect is known to be proportional to the applied energy fluence, as well as, the effective optical absorption coefficient of the interacting medium. Knowing all the above, we can now proceed to a more detailed analysis regarding the PA signal and the derivation of the general PA equation.

Derivation of the Photoacoustic equation

The general Photoacoustic (PA) equation can be derived from two fundamental equations. The first one is the thermal expansion equation [37] which is:

$$\nabla \vec{\xi}(\vec{r}, t) = -\kappa p(\vec{r}, t) + \beta T(\vec{r}, t) \quad (1.1)$$

Where $\vec{\xi}$ is the medium displacement vector during expansion, κ denotes the isothermal compressibility factor ($\kappa = -\frac{1}{V} \left(\frac{\partial V}{\partial p} \right)_T$), β the coefficient of volume expansion ($\beta = \frac{1}{V} \left(\frac{\partial V}{\partial T} \right)_p$), while p and T are the changes in pressure and temperature.

The second general equation is a specific form of Newton's second law of motion, the so called linear inviscid force equation, which is:

$$\rho \frac{\partial^2}{\partial t^2} \vec{\xi}(\vec{r}, t) = -\nabla p(\vec{r}, t) \quad (1.2)$$

in this equation the first term describes the mass density times the acceleration while the second term is the applied force per unit volume.

¹ http://molenergetics.fc.ul.pt/PAC_0055.html (last accessed on 21 September 2018)

And by taking the divergence of eq. 1.2:

$$\rho \frac{\partial^2}{\partial t^2} [\nabla \cdot \vec{\xi}(\vec{r}, t)] = -\nabla^2 p(\vec{r}, t) \quad (1.3)$$

One can substitute eq. 1.1 into the above and get:

$$\rho \frac{\partial^2}{\partial t^2} [-\kappa p(\vec{r}, t) + \beta T(\vec{r}, t)] = -\nabla^2 p(\vec{r}, t) \quad (1.4)$$

Or by re arranging terms:

$$\left(\nabla^2 - \kappa \rho \frac{\partial^2}{\partial t^2} \right) p(\vec{r}, t) = -\beta \rho \frac{\partial^2 T(\vec{r}, t)}{\partial t^2} \quad (1.5)$$

The speed of sound is expressed as: $u_s = \sqrt{\frac{1}{\kappa \rho}}$. Knowing that, equation (1.5) can be rewritten as :

$$\left(\nabla^2 - \frac{\partial^2}{u_s^2 \partial t^2} \right) p(\vec{r}, t) = -\frac{\beta}{\kappa u_s^2} \frac{\partial^2 T(\vec{r}, t)}{\partial t^2} \quad (1.6)$$

This is the general Photoacoustic (PA) equation that describes the generation and propagation of a PA wave within a medium. The left term represents the wave propagation while the right part represents the source term.

Thermal and stress confinement conditions

Under thermal and stress confinement two basic conditions should be satisfied:

- The laser pulse duration should be shorter than the thermal relaxation time:

$$t_L \ll \tau_{th} = \frac{d_c^2}{D}$$

where D is the thermal diffusivity and d_c is the characteristic dimension of the heated region

- The laser pulse duration is shorter than the stress relaxation time

$$t_L \ll \tau_s = \frac{d_c}{u_s}$$

Meaning that in thermal and stress confinement the laser pulse is so short, that the heat conduction and the pressure propagation during this time interval are negligible.

Under those conditions we can start from the fundamental energy equation:

$$Q = m C_V \Delta T \quad (1.7)$$

where Q is the thermal energy, m is the mass, C_V (J/kg·K) is the specific heat capacity under constant volume and T is the absolute temperature. Equation 1.7 can be rewritten in the form of:

$$\frac{dQ}{dt} = m C_V \frac{dT}{dt} = \rho V C_V \frac{dT}{dt} \quad (1.7)$$

By dividing both parts of 1.7 with volume (V), we can define a new quantity H called Heating function, denoting the thermal energy converted per unit volume per unit time (units: J/m³/s)

$$H = \rho C_V \frac{dT}{dt} \quad (1.8)$$

Laws of thermodynamics also indicate that

$$\frac{C_P}{C_V} = \frac{\kappa}{\beta_s} \quad (1.9)$$

where C_P and C_V are the specific heat capacities under constant pressure and volume respectively, whereas β_s stands for the isentropic compressibility, defined as:

$$\beta_s = -\frac{1}{V} \left(\frac{\partial V}{\partial P} \right)_S \quad (1.10)$$

The equation of state denotes that

$$u_s^2 = \left(\frac{\partial P}{\partial \rho} \right)_S \quad (1.11)$$

Combining equations (1.10) and (1.11):

$$\beta_s = -\frac{1}{V} \left(\frac{\partial V}{\partial P} \right)_S \frac{\partial \rho}{\partial \rho} = -\frac{1}{V} \left(\frac{\partial \rho}{\partial P} \right)_S \frac{\partial V}{\partial \rho} = -\frac{1}{V u_s^2} \frac{\partial V}{\partial \rho} = -\frac{1}{V u_s^2} \frac{\partial \left(\frac{m}{\rho} \right)}{\partial \rho} = \frac{1}{\rho u_s^2} \quad (1.12)$$

Therefore, from eq. (1.9) and (1.12), the isothermal compressibility factor can be rewritten as:

$$\kappa = \frac{1}{\rho u_s^2} \frac{C_P}{C_V} \quad (1.13)$$

The right part of equation (1.6) can now be re written, using (1.8) and (1.13) as:

$$-\frac{\beta}{\kappa u_s^2} \frac{\partial^2 T(\vec{r}, t)}{\partial t^2} = -\frac{\beta}{c_p} \frac{\partial H(\vec{r}, t)}{\partial t} \quad (1.14)$$

and now equation (1.6) can be expressed as:

$$\left(\nabla^2 - \frac{\partial^2}{u_s^2 \partial t^2} \right) p(\vec{r}, t) = -\frac{\beta}{c_p} \frac{\partial H(\vec{r}, t)}{\partial t} \quad (1.15)$$

Equation 1.15 can be further decomposed if we express the heating function as the product of its temporal and spatial term:

$$H(\vec{r}, t) = H_s(\vec{r}) H_t(t) \quad (1.16)$$

where the spatial term ($H_s(\vec{r})$) represents the source term (or the deposited energy J/m³), while the term $H_t(t)$ corresponds to the temporal impulse of the source (or the temporal excitation profile). Therefore, equation (1.15) becomes:

$$\left(\nabla^2 - \frac{\partial^2}{u_s^2 \partial t^2} \right) p(\vec{r}, t) = -\frac{\beta H_s(\vec{r})}{c_p} \frac{\partial H_t(t)}{\partial t} \quad (1.17)$$

If we have an impulse temporal excitation $H_t(t) = \delta(t)$ and thus the photoacoustic equation is expressed as:

$$\left(\nabla^2 - \frac{\partial^2}{u_s^2 \partial t^2}\right) p(\vec{r}, t) = -\frac{\beta H_s(\vec{r})}{c_p} \frac{\partial \delta(t)}{\partial t} \quad (1.18)$$

Photoacoustic pressure rise

An estimation regarding the generated PA pressure and temperature rise followed by pulsed laser excitation can be performed by taking into account the stress and thermal confinement conditions described earlier. Under those conditions, the fractional volume expansion is negligible and the term $\nabla \xi(\vec{r}, t)$ is equal to zero at the thermal expansion equation (1.1). Thus, if we assume that the illumination is homogeneous, immediately after the laser pulse the local pressure rise is:

$$p_o = \frac{\beta}{\kappa} T \quad (1.19)$$

And eq. 1.6 can also be expressed as:

$$\frac{Q}{V} = \rho C_V T \quad (1.20)$$

Eq 1.20 represents the thermal energy converted per unit volume and can also be written as a function of the specific optical absorption (A in J/m^3):

$$\frac{Q}{V} = \eta_{th} A = \rho C_V T \quad (1.21)$$

Where η_{th} is the percentage of the absorbed optical energy converted into heat and A is the specific optical power deposition/absorption ($A = \mu_a F$, where F stands for fluence (J/cm^2) and μ_a corresponds to the optical absorption coefficient for the employed wavelength). Therefore the temperature rise can be expressed as (using eq 1.21):

$$T = \frac{\eta_{th} A}{\rho C_V} \quad (1.22)$$

And the local pressure rise becomes:

$$p_o = \frac{\beta}{\kappa \rho C_V} \eta_{th} \mu_a F \quad (1.23)$$

By substituting (1.13) into (1.23) the PA pressure becomes:

$$p_o = \frac{\beta u_s^2}{c_p} \eta_{th} \mu_a F \quad (1.24)$$

We define the Grueneisen parameter (dimensionless) as:

$$\Gamma = \frac{\beta u_s^2}{c_p} \quad (1.25)$$

And finally the initial PA pressure can be written in a more compact form as:

$$p_o = \Gamma \eta_{th} \mu_a F \quad (1.26)$$

Therefore the initial PA pressure rise is expressed as a function of the incident optical fluence and the optical absorption coefficient, a wavelength depended parameter.

Non Linear PA generation

So far, we have described the generation of the PA signal under thermal and stress confinement conditions and derived the initial pressure rise equation. Under those conditions the initial pressure rise and the laser fluence exhibit a linear dependence. Nevertheless, there is a plethora of phenomena that can induce nonlinear relationships between the generated photoacoustic signal and the incident laser fluence value, such as optical saturation, temperature-dependence of thermodynamic parameters or photochemical reaction[38, 39]. As already mentioned the energy deposited by the laser pulse causes the heating of the material and subsequently its thermal expansion resulting in the production of the ultrasonic waves. Therefore, the photoacoustic generation can be expressed as a function of the laser fluence and the thermodynamics properties of the material (i.e. speed of sound, density, specific heat capacity, coefficient of thermal expansion β). The physical properties of a material are generally considered as constant parameters, but when the temperature rise is significant they can change dramatically initiating non linear effects. The most significant alteration and temperature dependence has been attributed to the thermal expansion coefficient β . The nonlinear contribution becomes significant when temperature rise is high enough to affect the value of β during the illumination. According to Calasso et al [39] the expression of the photoacoustic signal can be described by a linear term corresponding to the photoacoustic emission assuming that β had not changed in response to the temperature rise, and a nonlinear term attributed to the local temperature rise.

$$\beta = \beta_o + \beta_1 T$$

This non linear term introduces terms with temperature dependence of higher order in the PA equation.

Materials and Methods

Experimental Equipment

Laser System and Parameters

The system used for the laser cleaning trials was a BMI Q-switched Nd:YAG system (5022 DNS10 series, B.M. Industries, Le Plessis-Tréville, France) modified by IESL-FORTH to operate at the fundamental (1064 nm) and the third harmonic (355 nm) wavelengths individually and simultaneously [6]. The pulse width was 6.5 ns and the repetition rate used for our experiments was 1 Hz. The laser beams were focused to varying spot sizes in the range of approximately 2 mm x 3 mm as measured on black areas of a printed Black and white photographic paper. All irradiation tests were performed in dry conditions.

Experimental Setup

A schematic representation of the combined photoacoustic and optical experimental apparatus is shown in Figure 3. The ultrasonic transducer was fixed in a position at the corner of the sample, while the camera was positioned at a constant distance with an angle of approximately 45 degrees and focused on the irradiation spot. The laser beam was focused using a lens of $f=+20\text{cm}$ and the sample was placed in a distance of 15-17cm depending on the requirements of each experiment.

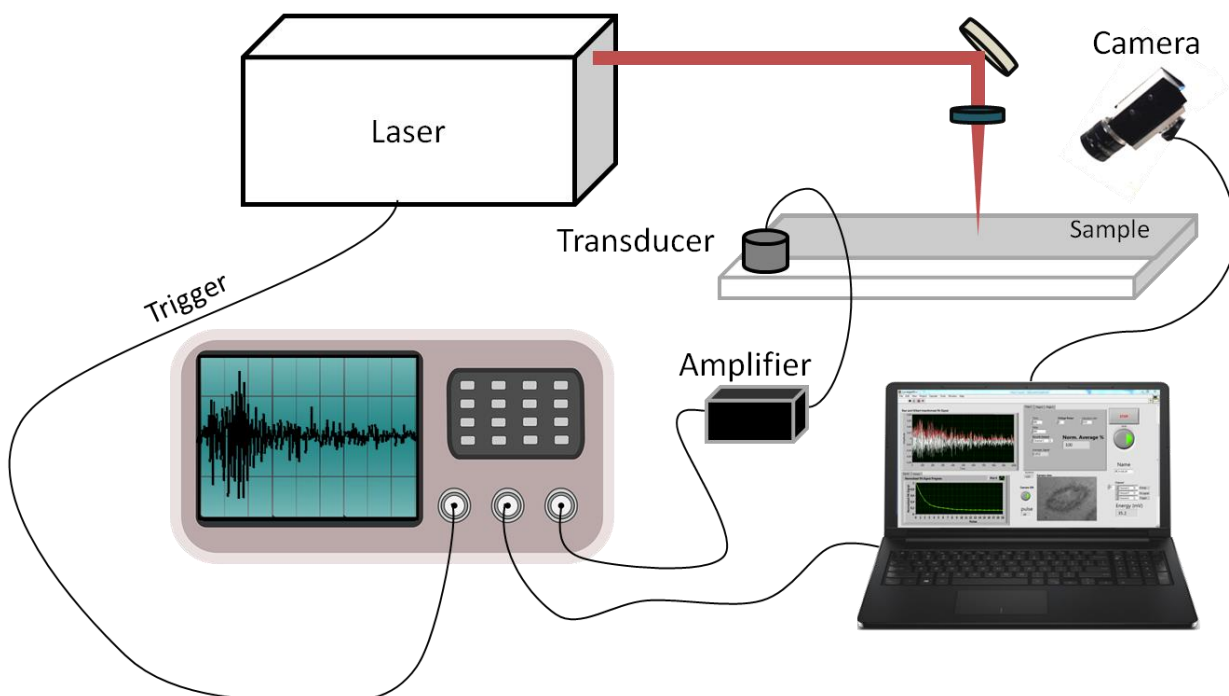


Figure 3: Schematic representation of the experimental set up

Hybrid Photoacoustic and Optical System

The hybrid photoacoustic and optical system was developed using the following equipment:

- Contact piezoelectric transducer: C110-RM Centrascan, Olympus, Japan; unfocused, central frequency: 5 MHz, 0.25 inch element diameter
- Low noise and high sensitivity RF amplifier: AU-1291, Miteq, USA; gain: 63dB
- High speed oscilloscope: DSO7034A, Agilent Technologies, USA; bandwidth: 350 MHz, maximum sample rate: 2 GSamples/sec
- CMOs Monochromatic Digital camera with resolution 5MPixel (iDs, UI-3480CP-M-GL), equipped with a C-Mount lens (focal length 35mm – Edmund Optics).
- Computer with the custom developed software in LabView

In order to control the system a custom software was developed in LabVIEW environment. The laser trigger is synchronized with the custom made system and a number of parameters could be adjusted by the user, depending on the needs of the experiment. Initially, a detection limit is set in order to separate the noise/trigger signal of the system from the intrinsically generated acoustic waves generated during the laser ablation. When this limit is surpassed, the signal is detected by the transducer and a high resolution digital image is recorded. The signal is then transmitted to the amplifier, and is digitized through the oscilloscope. The latter is connected with a computer and the initial waveform can be observed through the custom made software. The mean amplitude of the PA signal is obtained after the Hilbert transformation of the waveform is performed. The temporal window in which the signal is recorded can be individually selected by the user, while the waveform is always sampled using 1.000 points. The procedure is repeated for each incident laser pulse on the ablation spot while the data are recorded in .txt and .xls format.

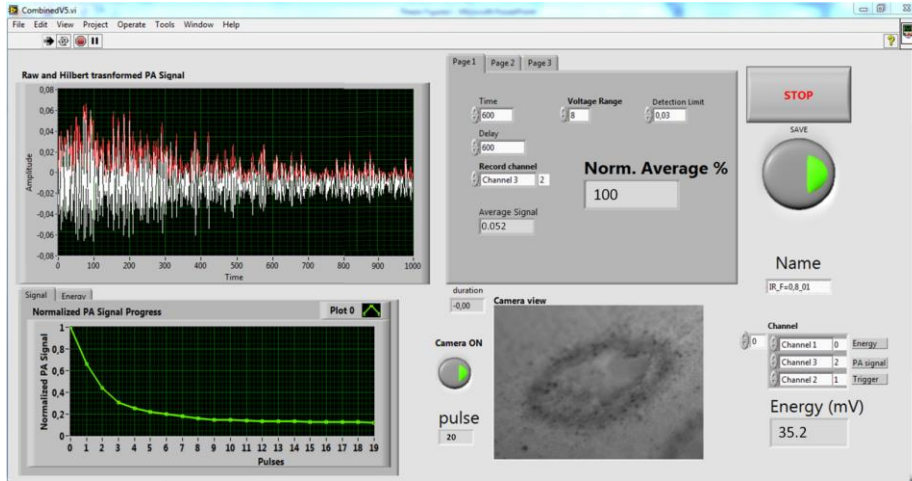


Figure 4: Custom made software for the photoacoustic and optical monitoring system. The program is developed in LabView environment.

Through the program the user can select the recording parameters depending on the needs of the experiment. An image from the interface while the system is operating is presented in Figure 4. Apart from the detection limit (usually set at 0.03mV) which was mentioned before, the user can also set the detection temporal window (600 microseconds in Fig. 4) and the delay time before the detection of the signal, depending on the relative distance between the irradiation point and the transducer (also usually set between 600 and 100 microseconds). Typically, these parameters are optimized at a test spot before the initiation of each measurement. For every incident laser pulse the information provided to the operator in the front panel are:

- The obtained time domain PA waveform presented with a white line in Figure 3 along with its Hilbert transform (red line in Figure 4).
- The energy of the laser beam measured in millivolts
- An image of the irradiated spot from the camera
- The normalized signal progress
 - for each pulse the mean amplitude of Hilbert transform is calculated, by averaging its modulus across the 1,000 points used to sample in the selected temporal window
 - the procedure is repeated for each laser pulse and the values are normalized to the maximum among them

At the end of each measurement, four individual files are saved including the recorded and calculated data. Due to fluctuations in the pulse energy of the laser beam which could affect the measurements, an additional normalization was performed. The recorded energy values were normalized to the maximum among them and then the outcome was used for the normalization of the calculated mean PA amplitude. Following this normalization procedure, the energy fluctuations of each laser pulse, especially regarding the UV wavelength, were minimized at a point which didn't practically affect the recorded PA signal and thus the outcome of our measurements.

Recording protocol

A specific methodology/recording protocol was developed during the performed experiments in order to extract accurate and reliable results. The methodology described hereafter was adjusted to meet the needs of the different irradiation experiments that will be presented in the following section. The measurements were performed with the transducer fixed in the corner of the sample and the delay time adjusted for every irradiation spot. The distance among the spots was kept constant at 4mm; a schematic representation of the experimental configuration is presented below (Figure 5). The number of pulses applied to the surface was kept the same for each irradiation spot for consistency purposes. In this way it was possible to ensure that relative distance of the analyzed spots from the transducer is the same and the entire generated waveform was recorded. Every measurement was repeated a number of times in order to extract statistically reliable results.

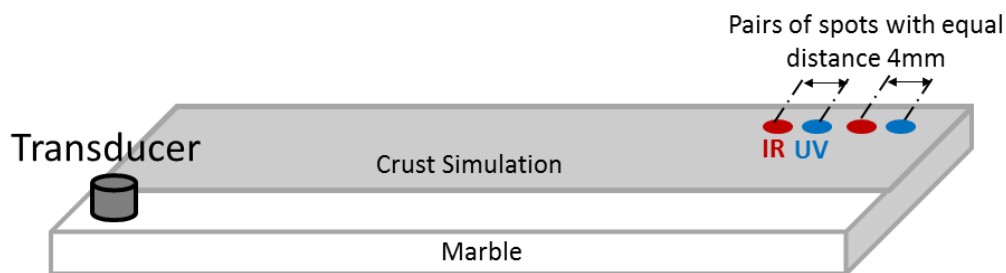


Figure 5: Geometry of the irradiation methodology during the experiments.

Experimental Techniques

SEM

Characterization of the sample's surface was performed by Scanning Electron Microscopy (SEM) at the Department of Biology of the University of Crete, using the JEOL JSM - 6390 LV model at 15 kV and with a resolution of 3nm (figure 6). The irradiated samples were coated with a-10 nm gold (Au) film using the sputtering technique before observation under SEM.

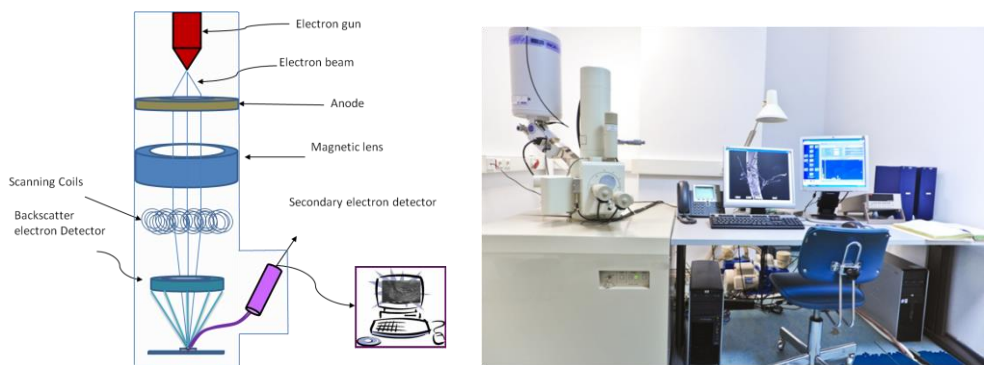


Figure 6: SEM set up (left) and JEOL JSM – 6390 LV (right).

Briefly, SEM is a microscopy technique which uses electrons instead of light to record an image. SEM images the sample surface by scanning it with a high-energy beam of electrons in a raster scan pattern. The electrons interact with the atoms that make up the sample producing signals that contain information about the sample's surface topography, composition. In a typical SEM, an electron beam is thermionically emitted from an electron gun fitted with a tungsten filament cathode. The electron beam, which typically has an energy ranging from a few hundred eV to 40 keV, is focused by one or two condenser lenses to a spot about 0.4 nm to 5 nm in diameter. The beam passes through pairs of scanning coils in the electron column, which deflect the beam in the x and y axes so that it scans in a raster fashion over a rectangular area of the sample surface.

Profilometer

The profilometer system was Perthometer S5P (Mahr, Göttingen, Germany), and is presented in Figure 7. Through profilometry, the thickness of the ablated material was measured. For statistically representative results, each measurement was repeated a number of times and the results presented correspond to the average calculated values along with their standard deviation.

The stylus of the profilometer is free to move in a vertical plane and drawn by the tracer along a measuring path. The movements of the stylus tip are transferred to an electrical measuring value converter where they are transformed into voltage values portraying the traced profile. The drive unit moves the tracer with a constant speed along a horizontal path over the surface to be measured. The measuring amplifier achieves the necessary vertical magnification of the traced profile. The microcomputer determines the results for all surface parameters during the tracing process. The traced profile and selected measuring results are automatically printed. The measuring documentation contains the profile diagram, measuring results along with data of the measuring units.

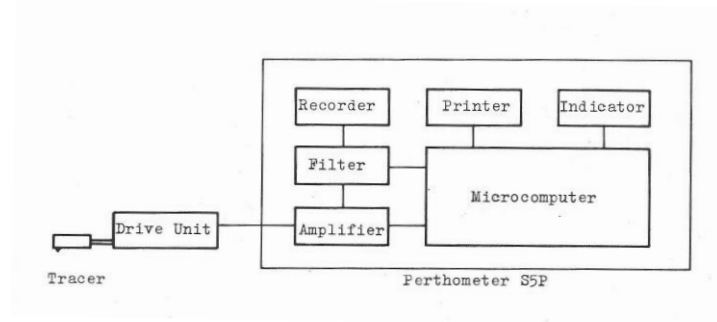


Figure 7: Schematic representation of profilometer system.

UV-VIS spectrophotometer

The reflectance spectra of the specimens were recorded by a Perkin-Elmer Lambda 950 ultraviolet-visible spectrophotometer. The reflection as a function of wavelength was measured with a resolution of 1 nm in the spectral range of 300-1200 nm. A background spectra was recorded prior the measurements for calibration purposes using a Spectralon diffuse reflectance standard. The LAMBDA 950 (Figure 8) consists of a double beam optical system, two light sources (deuterium and tungsten-halogen lamps), a double monochromator, a photomultiplier R6872 for the detection in the UV/VIS range and a Peltier cooled PbS detector for the NIR region. The data acquisition is controlled by a personal computer. The UV/Vis resolution reaches 0.05nm, while the NIR resolution reaches up to 0.20nm.

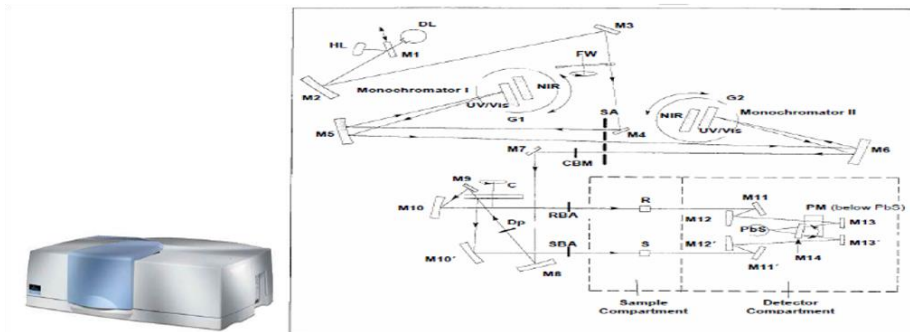


Figure 8: Lambda 950 spectrophotometer

Samples

Marble Samples Description

A commercial marble variety, commonly encountered in Greece, was used for our experiments. The marble samples were provided by the local company Stonetech Gonianakis. According to the manufacturer, they were from the variety Thassos White quarried from the homonymous island in Northern Greece. It is a pure white, medium to coarse grained marble, with visible grains. Slabs of 14 cm x 7 cm x 1 cm were used for the performed cleaning tests, while some smaller slabs of 4 cm x 4 cm x 1 cm were used to determine the damage thresholds of the marble and for selected experiments evaluated with SEM. The specifications as provided by the supplier are listed in the following tables.

Physical and mechanical properties

Flexual strength	12.00MPa
Absorption Coefficient	0.14%
Open porosity	0.38%
Apparent Specific weight	2830kg/m ³
Abrasion resistance	3.51mm
Compressive strength	95.00 MPa

Mineralogical Composition (Weight %)

Calcite	12
Dolomite	86
Quartz	2

Chemical Analysis (Weight %)

CaO	34.00	K₂O	0.02
MgO	20.00	Na₂O	0.03
SiO₂	0.07	MnO	0.02
Fe₂O₃	0.12	CO₂	46.20
Al₂O₃	0.22		

Sample Preparation

Experiments were carried out on simplified technical simulation samples of marble with environmental crust. The samples were made from marble soiled with a mixture of gypsum and carbon. Two different kinds of soiling were applied to the marble slabs. Most of them were covered with layers of varying thickness of gypsum mixed with 5% w/w Carbon in the form of charcoal particles. One sample was prepared from a mixture of Carbon with 13.5% w/w in gypsum. The gypsum was in the form of pure hemihydrate provided by a chemical company (95% purity Sigma Aldrich), and the Carbon by Fluka Chemica. The mixture was hydrated using distilled water while the samples were left to dry for at least 48 hours, prior to any experiment.

Results

Ablation and Extraction Thresholds

Prior to the experiments conducted with the developed PA system, the ablation and extraction threshold for the marble substrate and the crust simulation were determined. The ablation study was performed for irradiation with 1064 and 355 nm and evaluated with SEM and profilometry. This study aimed at the determination of the laser parameters that correspond to 3 different irradiation results: optimum cleaning, damage (due to over-cleaning) and inefficient crust removal. The determined conditions were afterwards studied with the optical and PA system, with the aim to demonstrate its potential as a monitoring tool.

Marble Ablation Thresholds

Initially the ablation thresholds of marble were determined. For this purpose, a series of spot irradiation experiments were performed on the reference surface of the sample, with each wavelength individually. The ablation threshold corresponds to the lowest fluence value that induces physical changes on the material and it is calculated by recording any modification on the surface of stone/mineral (color changes, texture modifications, grain extraction etc.) upon single and multi-pulse irradiation at increasing fluence values. The determination of the ablation thresholds was accomplished by means of Optical Microscopy (Dino Light microscope), micro - Profilometry and Scanning Electron Microscopy. The ablation threshold study, as well as, the rest of the experiments of this thesis, was performed in the polished side of the marble slabs. For the 1064nm the fluence values tested ranged from 0.65 J/cm² up to 1.4 J/cm² while for the 355nm ranged from 0.5 J/cm² up to 1.0 J/cm². The determined ablation thresholds are presented in the table below.

Wavelength	Ablation threshold (J/cm²)
1064nm	0.8
355nm	0.5

Table 1: Marble ablation thresholds for 1064 and 355nm

The ablation threshold has been determined to be 0.8 J/cm² for the 1064nm wavelength, as no alteration has been observed at the surface after irradiation with 20 laser pulses, also confirmed by SEM. For reference purposes, images from irradiation conditions above the material's thresholds are also shown (Figures 10, 11 and 12). In this case, it is easy to observe the material extraction, as well as, the laser induced damage at the surface even after a single laser pulse.

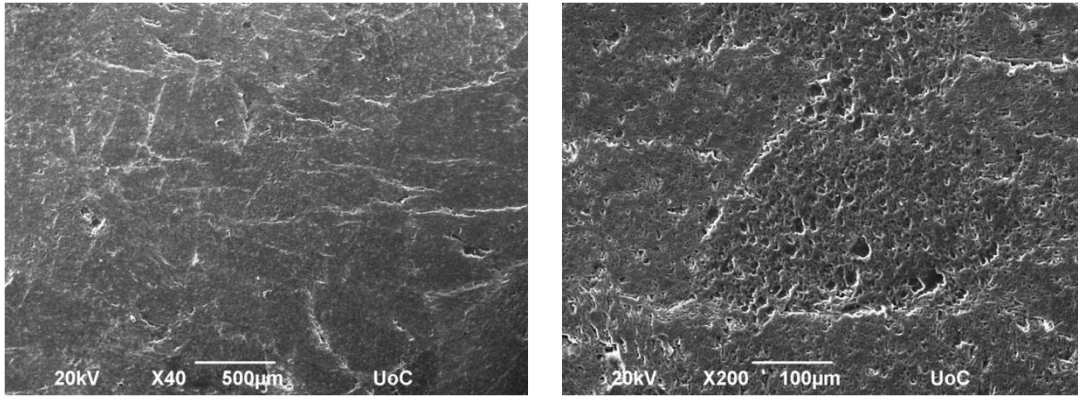


Figure 9: SEM image of the reference marble surface before any irradiation experiment.

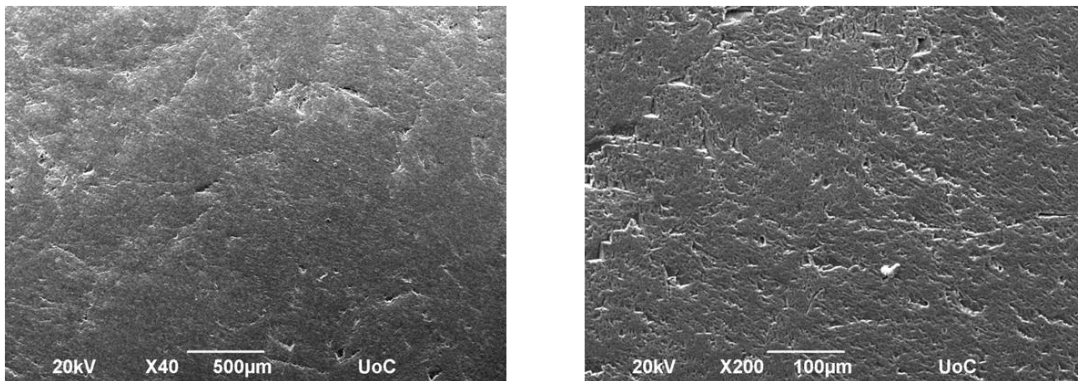


Figure 10: SEM image of the reference marble surface after irradiation with 20 pulses of $F=0.8 \text{ J/cm}^2$ at 1064nm. The fluence value of 0.8 J/cm^2 has been determined to be the ablation threshold of the marble for the IR wavelength.

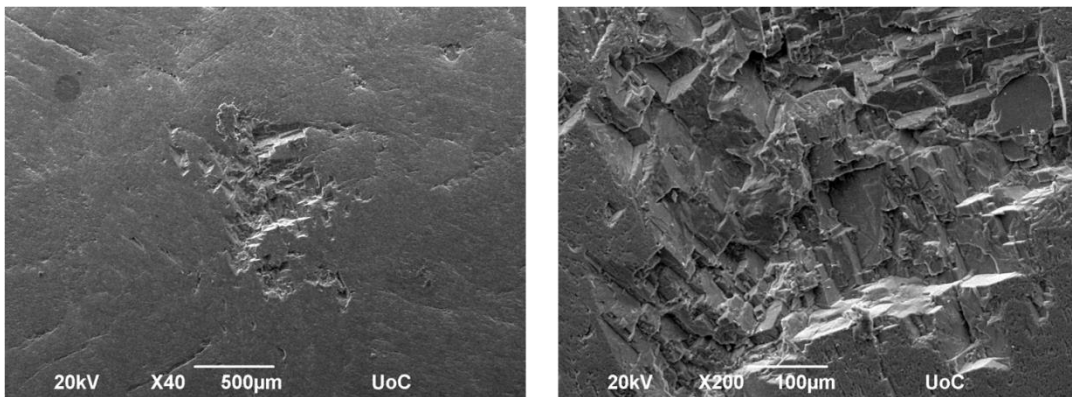


Figure 11: SEM image of the reference marble surface after irradiation with 1 pulse of $F=1.0 \text{ J/cm}^2$ at 1064nm. This irradiation condition exceeds the ablation threshold of the material.

A similar procedure was repeated for the wavelength of 355nm; again selected images of the surface below and above the ablation threshold are presented (Figures 13 and 14). For reference purposes, regarding the condition above the threshold, images after single pulse irradiation with 1.0 J/cm^2 has been selected to be shown.

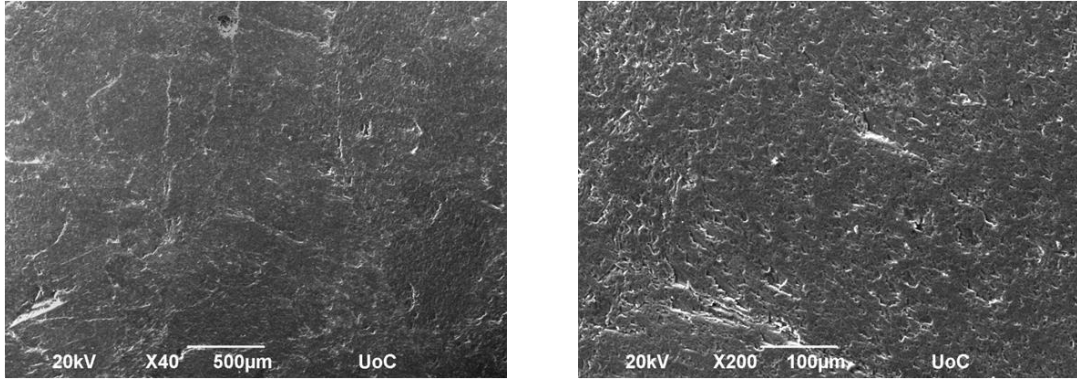


Figure 12: SEM image of the reference marble surface after irradiation with 20 pulses of $F=0.5 \text{ J/cm}^2$ at 355nm. The fluence value of 0.5 J/cm^2 has been determined to be the ablation threshold of the marble for the UV wavelength.

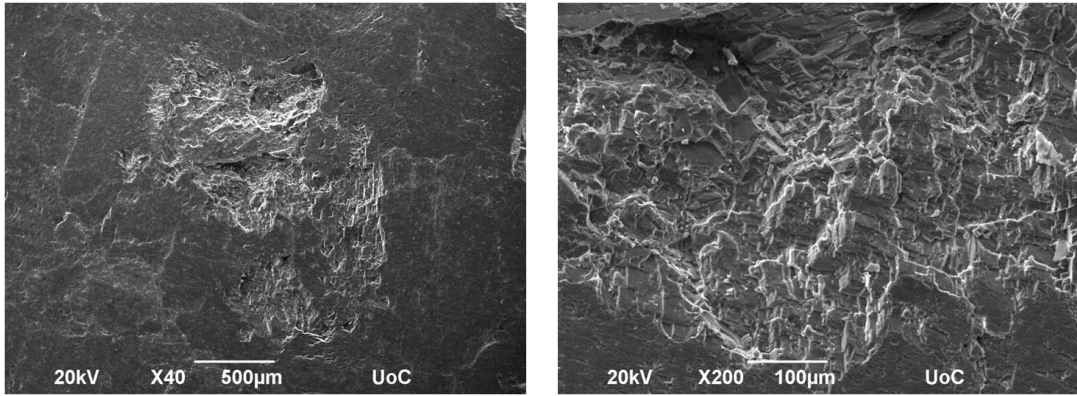


Figure 13: SEM image of the reference marble surface after irradiation with 1 pulse of $F=1.0 \text{ J/cm}^2$ at 355nm. This irradiation condition exceeds the ablation threshold of the material.

Artificial Crust Extraction Thresholds

The extraction thresholds of the crust simulation have also been calculated. Due to the low fluence value required to ablate the crust material, a direct measurement of the extraction threshold was not feasible. Fluence values ranging from 0.1 J/cm^2 up to 1.1 J/cm^2 were tested for both wavelengths. Still, the threshold for each individual wavelength has been calculated by measuring the pulse energy for every fluence value used, along with the corresponding spot size, as recorded on the surface of the crust after single pulse irradiation. For Gaussian beams, Liu et al [40] reported that the threshold energy (E_{thr}) can be calculated through the semi logarithmic plot of the energy (E) dependence on the spot size (of d diameter). The beam radius w_0 , at the $1/e$ of the Gaussian beam distribution, corresponds to the slope of the linear fit of the data, while the intercept at the value of threshold Energy described by the relationship: $d^2 = 2w_0^2(\ln(E_{\text{thr}}) - \ln(E))$. The measurement of the spot size was performed with Dino light microscope; selected photos for the IR and UV wavelengths are presented in Figure 15-18. Following the same protocol, the extraction threshold for the IR wavelength has been calculated to be $F_{\text{thr_IR}} = 0.04 \text{ J/cm}^2$, while for the UV wavelength $F_{\text{thr_UV}} = 0.02 \text{ J/cm}^2$.

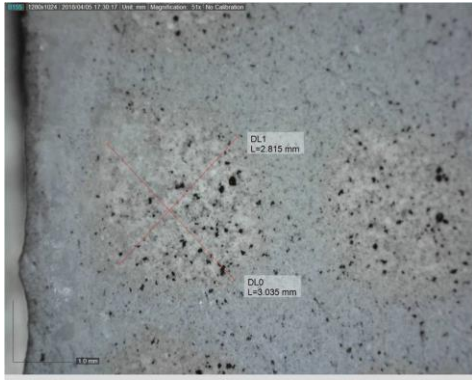


Figure 14: Measured spot size on simulation crust sample after 1 pulse of $F=1.0 \text{ J/cm}^2$ at 1064nm.

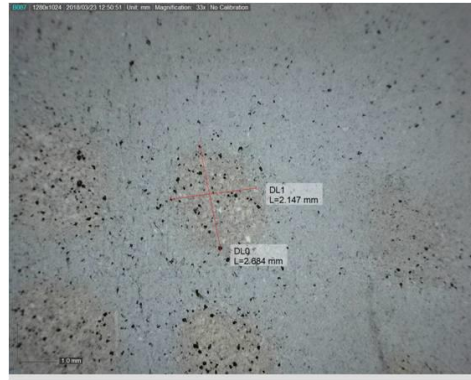


Figure 15: Measured spot size on simulation crust sample after 1 pulse of $F=0.5 \text{ J/cm}^2$ at 1064nm.



Figure 16: Measured spot size on simulation crust sample after 1 pulse of $F=1.0 \text{ J/cm}^2$ at 355nm.



Figure 17: Measured spot size on simulation crust sample after 1 pulse of $F=0.3 \text{ J/cm}^2$ at 355nm.

Non Linear PA effect - Ablation coefficients

The next step of this research was the investigation of the dependence of the PA signal on the incident laser fluence values. A direct measurement of the temperature dependence of the thermal expansion coefficient, and the rest physical parameters of the involved materials, was not feasible. Still the onsets of non linear behavior could be defined through a measurement of the generated PA signal for gradually increasing fluence values. In this manner, the fluence regime where non-linear temperature dependence is dominant could be defined. In general, the dependence between the generated PA signal and the temperature rise can be determined by investigating the behavior of the following equation:

$$p_o = \frac{\beta}{\kappa}T \text{ and } \beta = \beta_0 + \beta_1T \text{ from which we get } p_o = \frac{1}{\kappa}(\beta_0 + \beta_1T)T$$

For the realization of those experiments, the maximum PA amplitude has been studied, for a number of increasing Fluence values of both individual wavelengths. The investigated sample was a simulation of encrustation layer made from Gypsum with 5% w/w Carbon. In order to ensure the accuracy of the measurements, each point is represented by the mean value of the mean PA amplitude from five different spots, while the error bars represent the standard deviation of the measurement. The transducer was fixed on the corner of the sample throughout the measurement so that the relative distance of each spot from it is approximately the same.

Those results show that the ablation coefficients for varying F values do not present a linear behavior; instead they are characterized by second order polynomial dependence. Nevertheless, it was possible to identify a low fluence regime where the relationship among the PA signal and F is approximately linear. In the graphs presented below the results for both IR and UV wavelengths are shown.

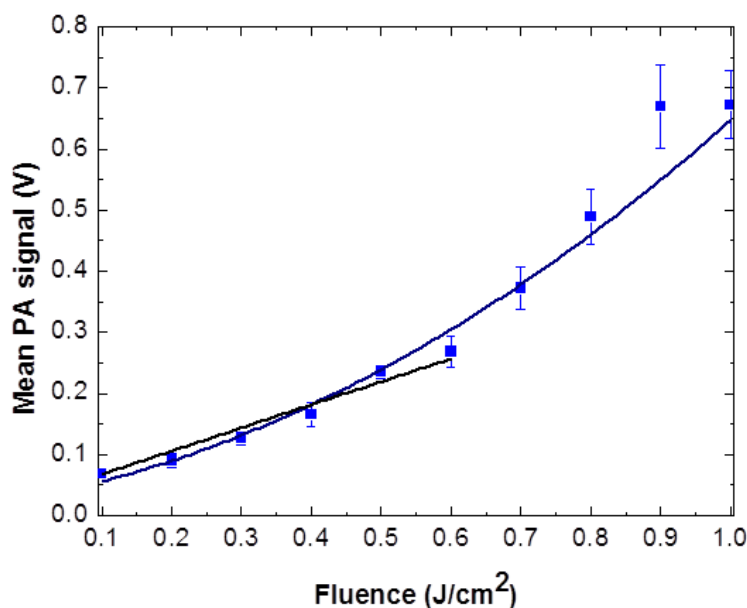


Figure 18: Mean PA signal for varying Fluence values for the 355nm laser beam. The black line corresponds to the polynomial fit of the data, while the red to the linear fit in the low F regime. The error bars represent the standard deviation.

The fitting of the data regarding the UV wavelength are provided in the table below

Model	Polynomial	$y=a+B_1*x+B_2*x^2$	
Adj. R-Square	0.99051		
		Value	Standard Error
Mean	Intercept	0.03	--
Mean	B₁	0.21923	0.03192
Mean	B₂	0.39762	0.05889

Table 2: Polynomial fit of the data at 355nm

The intercept in both cases has been fixed at 0.03 V (similar to the detection limit of our system) and represents the noise background of acoustic detection. By equalizing the first and second order term of the polynomial equation it is possible to determine the F value for which the contribution of both linear and non-linear terms becomes comparable. Therefore, it is safe to assume that for fluence values below this level the linear term is dominant and the PA signal is directly proportional to the laser induced temperature rise. The linear fit of the data has been performed in the F regime of 0.1-0.6 J/cm² due to the fact that from F=0.55 J/cm² and above, the non-linear term is dominant.

Equation	$y = a + b*x$		
Adj. R-Square	0.99107		
		Value	Standard Error
Mean	Intercept	0.03	--
Mean	Slope	0.37819	0.01388

Table 3: Linear fit at 355nm

Similarly, regarding the IR irradiation wavelength, a respective graph demonstrating the dependence of PA as a function of incident fluence can be generated (Figure 20).

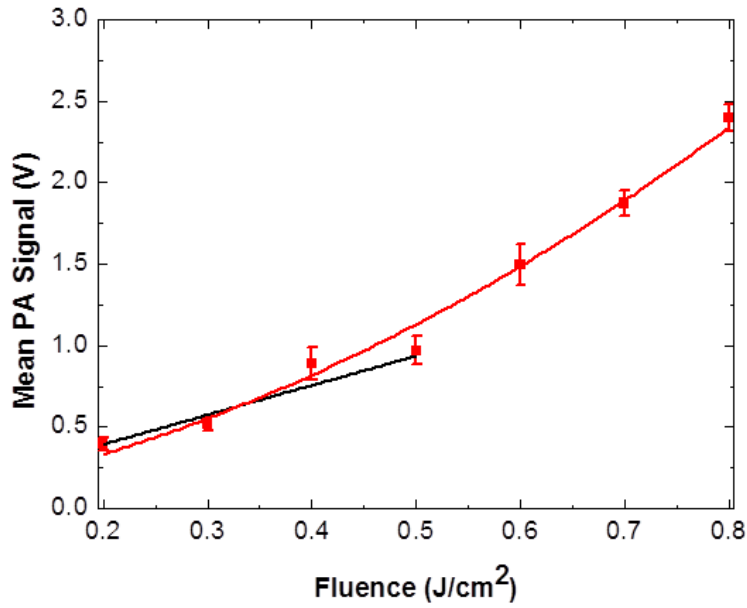


Figure 19: Mean PA signal for varying Fluence values for 1064nm. The red line corresponds to the polynomial fit of the data, while the black to the linear fit in the low F regime.

Model	Polynomial	$y=a+B_1*x+B_2*x^2$	
Adj. R-Square	0.99454		
		Value	Standard Error
Mean	Intercept	0.03	--
Mean	B₁	1.06071	0.17034
Mean	B₂	2.28245	0.27258

Table 4: Polynomial fit data at 1064nm

The linear fit of the data has been performed in the fluence regime of 0.2-0.5 J/cm², as from F=0.45 J/cm² and above, the non-linear term becomes dominant.

Equation	$y = a + b*x$		
Adj. R-Square	0.98973		
		Value	Standard Error
Mean	Intercept	0.03	--
Mean	Slope	1.81455	0.09174

Table 5: Linear fit at 1064nm

Therefore, for both wavelengths a regime of low F values that are linearly dependent from the PA has been determined. As expected the upper fluence value of the linear

regime is higher for the UV wavelength compared to the IR, given that infrared radiation is usually associated with stronger thermal effects and higher temperature rise. Furthermore, the associated laser ablation mechanisms can be investigated in the low fluence regime where F and T present a linear behavior.

Comparison of the generated PA signal for marble and carbon

On this basis, the difference in the laser induced temperature rise regarding the simple materials involved in this project can be estimated. The materials selected are marble and Carbon as they represent a simplified example of substrate and encrustation layer. Due to technical difficulties, (the carbon is in powder form) direct measurements on a pure Carbon sample could not be performed and thus, a sample containing a low quantity of gypsum (13.5% w/w) as a binding medium was prepared. The thermal conductivity, specific heat capacity and the density of each material are known and can be found in a variety of papers or databases. The values of the thermal and optical parameters of the specimen (Carbon with 13.5% Gypsum) were given by the weighted combination of the two components, and are listed in the table below.

For temperature of 25°C	Marble	Carbon	Gypsum	Carbon with 13.5% w/w Gypsum
Cv (kJ/kg K)	3.344 [41]	1.062	1.01 [42]	1.06
ρ (g/cm ³)	2.83	2 (manufacturer)	2.31	2.04
β (10 ⁻⁶ K ⁻¹)	12.9 [43]	4.5[44]	6.96 [45]	4.82

Table 6: Thermal and physical parameters of Marble, Carbon and Gypsum

Therefore, for a specific fluence value and wavelength:

$$\frac{p_{carbon}}{p_{marble}} = \frac{\left(\frac{\beta}{k\rho C_V} \eta_{th} \mu_a F\right)_{carbon}}{\left(\frac{\beta}{k\rho C_V} \eta_{th} \mu_a F\right)_{marble}}$$

Assuming that all the absorbed laser energy is converted into heat for both materials, and that the irradiation is performed with the same F value we get:

$$\frac{p_{carbon}}{p_{marble}} \propto \frac{(\mu_a)_{carbon}}{(\mu_a)_{marble}} \quad (7)$$

From the above it can be observed that the ratio of the generated PA signal for the selected materials can be determined through the ratio of the absorption coefficients. In the specific work, instead of measuring the absorption coefficient of the involved materials, the relative absorption was measured, using the spectrophotometer (Figure 21).

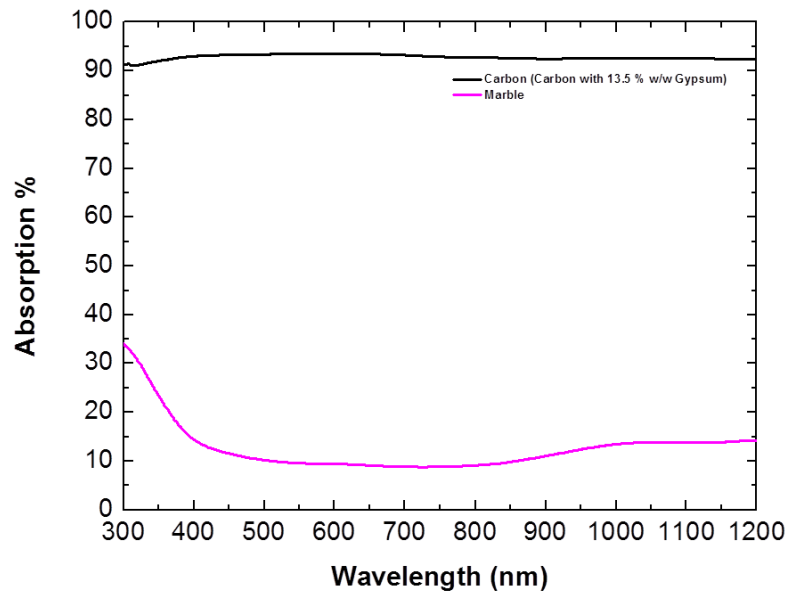


Figure 20: Absorption Spectra of Carbon (with 13.5% w/w in Gypsum, black line) and Marble (red line)

Using the relative absorption as measured for the wavelength of 1064nm equation (7) becomes:

$$\left(\frac{p_{carbon}}{p_{marble}}\right)_{1064nm} = 6.27$$

Therefore the expected ratio for the generated PA signal for linear regime upon irradiation of marble and carbon is expected to be 6.27.

In order to evaluate this result the sample was irradiated with a fluence value of 0.1 J/cm² at 1064nm. The transducer was kept fixed at the corner of the sample while the distance among the irradiation spots was approximately 4mm. In order to have a statistically representative sample the measurement was repeated 2 times, while each ratio is the average from 6 pairs of spots. Through those measurements the PA signal

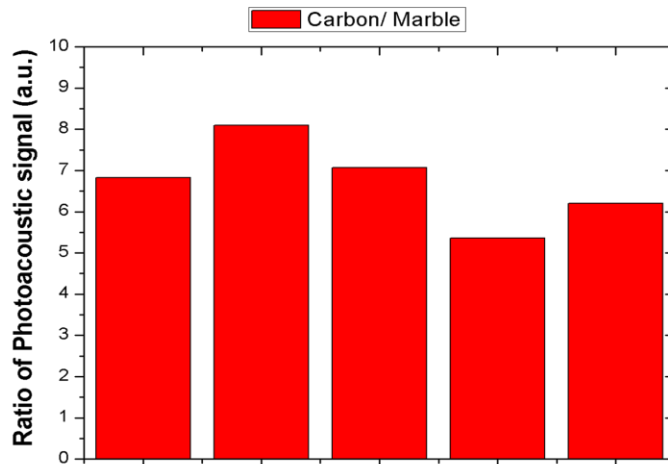


Figure 21: Measured ratio of Carbon/Marble PA signal generated upon irradiation with F=0.1 J/cm² at 1064nm

ratio was found to be:

$$\left(\frac{p_{carbon}}{p_{marble}}\right)_{1064nm} = 6.711 \pm 1.02$$

Comparing the results obtained through the direct measure of the PA signal ratio and the calculated ratio using the spectrophotometer measurements it can be seen that the difference is 12 %.

Estimation of the local Temperature rise

During the ablation of a material using a nanosecond laser in the IR regime the mechanism that prevails is the photothermal. An estimation of the temperature rise during the ablation process is feasible using the following equation (described analytically in the theory)

$$T(t) = \frac{2 a I}{K} \sqrt{\frac{kt}{\pi}}$$

Using this simple model, the temperature rise during the laser irradiation can be calculated, if the thermal parameters of the material are known (Table 9).

1064nm			
For temperature of 25°C	Marble	Carbon	Gypsum
D (W/mK)	4.72	1.7	1.26
Cv (kJ/kg K)	3.34	1.06	1.01
ρ(g/cm³)	2.83	2.00	2.31
α (%)	0.17	0.92	0.11

Table 7: Thermal and optical parameters of Marble and Carbon for the wavelength of 1064nm.

The calculated temperature rise during irradiation with a Nd:YAG laser at 1064nm, with pulse duration of 10ns and a Fluence value of 0.1 J/cm² is approximately 4000°C, as shown in the table below.

1064nm			
	Marble	Carbon	Gypsum
T (°C), 10ns	613	4005	430
T (°C) from literature, 10ns[4]	1061	5232	
T (°C) from literature, 20ns	750	3700	-

Table 8: Calculated temperature rise for marble and Carbon during irradiation with F=0.1 J/cm² at 1064nm and with pulse duration of 10ns. Also literature values are presented for comparison.

As can be observed, the calculated temperature rise values are of the same order of magnitude with the ones known by the literature. The calculation of temperature rise regarding the literature value for the pulse duration of 10ns was performed with a simple mathematical reduction. Deviations among the calculated and the literature values can be attributed to the values used for the thermal and optical parameters.

PA signal and Laser Induced Ablation Mechanisms: Comparison between 1064 and 355nm

Knowing all the above, we can now proceed to a discussion regarding the generated photoacoustic signal using an IR and a UV wavelength. As already mentioned in the theory section, each wavelength induces different ablation mechanisms through which the material is extracted. In general, longer wavelengths (i.e. IR) have low photon energy, incapable of direct bond breaking, and the energy is predominantly converted into heat, through collision processes. Assuming that all of the incident laser energy is converted into heat, $\eta_{th} = 1$ a calculation for the ratio of the laser induced temperature can be achieved. Using the initial photoacoustic pressure rise equation (linear regime):

$$p_o = \frac{\beta}{\kappa} T$$

We get that

$$\frac{p_{IR}}{p_{UV}} = \frac{\left(\frac{\beta}{\kappa} T\right)_{IR}}{\left(\frac{\beta}{\kappa} T\right)_{UV}} = \frac{T_{IR}}{T_{UV}}$$

For the realization of the measurements the transducer was fixed in the corner of the sample, and a total of 25 pair of spots were analyzed. Each pair of spots consists of one spot irradiated with 20 pulses of 1064nm and one irradiated with 355nm with a selected F value, equal for both wavelengths.

The irradiation was performed in the linear fluence regime with values typically used in laser cleaning applications. The temperature ratio was calculated by the 1st incident pulse to the marble interacting with the original material. Subsequent pulses incident on the surface encounter a material with modified/altered physicochemical properties (color, absorption, etc.). A characteristic example from a measurement performed with $F=0.5 \text{ J/cm}^2$ for both individual wavelengths is presented below. Initially, the optical images recorded after every incident laser pulse (Figure 22) can be seen. The existence of distinct ablation mechanisms for each irradiation wavelength can be primarily confirmed by the different color of the irradiation spot.

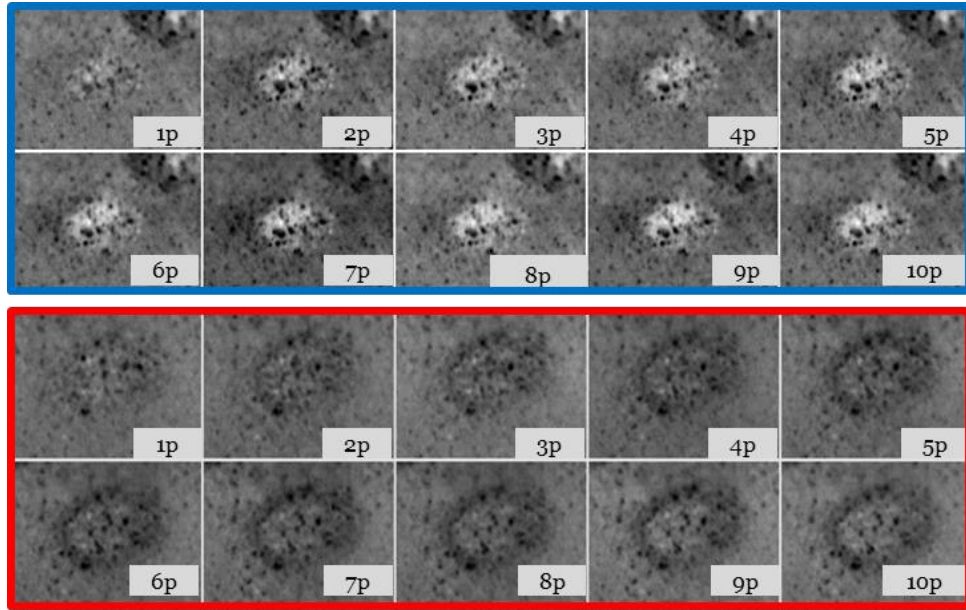


Figure 22: Recorded images for the 10 first incident pulses of $F=0.5 \text{ J/cm}^2$ at 355 (blue) and 1064nm (red).

In the following graph (Figure 23), the corresponding evolution of the mean amplitude of the recorded PA signal is presented.

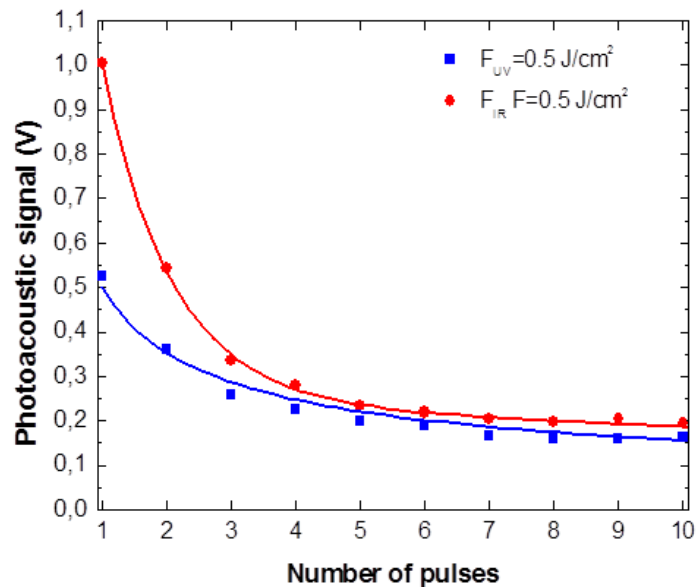


Figure 23: Mean amplitude of the recorded PA signal for 10 incident laser pulses. The irradiation was performed with 1064 and 355nm at fluence value 0.5 J/cm^2 .

As can be observed, the maximum amplitude of the recorded PA signal reaches a plateau after the first 7 incident laser pulses, indicating attenuation at the material extraction rate, although the marble substrate has not been reached. This result can be associated with the modification of the material properties induced by the selective laser ablation, since as more pulses are applied, the material no longer absorbs/

interacts with the laser pulses, and thus the ablation process ends, as can also be confirmed by the recorded images.

Using a robust statistical analysis protocol, developed in Matlab environment, an empirical power fitting of the data was performed ($y=a*x^{-b}$, where x is the pulse number and y the PA signal) for each pair of spots (and a total of 25 pairs). The fitting was performed with the method of nonlinear least squares. To minimize the influence of outliers the data were also fit using robust least squares regression and in specific with bisquare weights method. This minimizes a weighted sum of squares as the weight is given to each data point depends on how far the point is from the fitted line. The results that will be presented hereafter represent their average values. The fitting was characterized by high adjusted R^2 values, confirming the fitting quality of the selected model, and in specific with $R^2_{IR} >0.99$ and $R^2_{UV} >0.99$. In brief a characteristic example from the results of a measurement is presented in the table below:

Mean value $y=a*x^{-b}$	IR	UV
b	0.885 ± 0.1453	0.5702 ± 0.0490
a	1.099 ± 0.236	0.537 ± 0.074
R^2	0.990 ± 0.007	0.986 ± 0.007
1st – 2nd pulse difference	$45.5 \% \pm 4.9\%$	$26.8 \% \pm 5.0304 \%$
IR/ UV b ratio	1.551 ± 0.262	
IR/UV a ratio	2.087 ± 0.5868	

Table 9: Empirical fitting for a measurement of 25 pairs of spots

In addition, the PA amplitude recorded for the IR ablation is approximately twice the one recorded for the UV wavelength in Figure 23. This is further verified through the statistical analyses performed, where the mean PA signal for the IR 1st pulse value has been calculated to be $1.073 \text{ V} \pm 0.068 \text{ V}$ and the mean for the UV 1st pulse value $0.527 \text{ V} \pm 0.048 \text{ V}$. The mean paired ratio of 1st pulse value was $IR/UV = 2.051 \pm 0.207$.

The relative IR/UV ratio of the 1st pulse value is approximately equal to ~ 2 , thus indicating that the temperature rise during the ablation with IR is two times higher than the temperature rise during UV laser. Consequently, confirming that different ablation mechanisms are induced by each individual wavelength; the use of 1064nm results into more intense thermal effects in comparison to the 355nm.

Furthermore, ablation with the 1064nm seems to generate significant changes in the material properties. This is shown through the amplitude variation among the 1st and

2nd pulse regarding the IR which is 45%, in comparison to the UV which exhibits a variation of only 26%.

In order to further confirm and evaluate these results, the reflectance spectra of the materials involved in this research was recorded prior and after irradiation with 1 pulse of the selected conditions. The results are presented below.

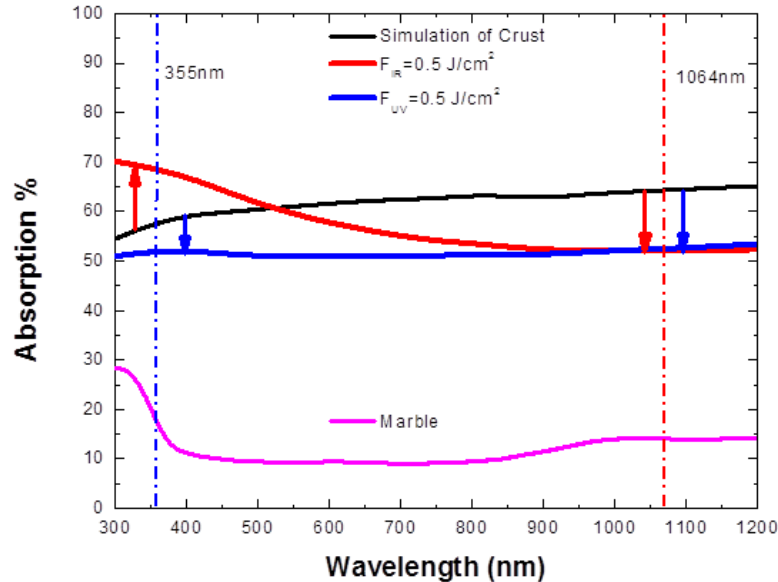


Figure 24: Absorption spectra of the investigated samples before and after irradiation with 1 pulse of $F=0.5 \text{ J/cm}^2$ at 1064 and 355nm.

From Figure 24 it can be observed that when the simulated crust is irradiated with 1 pulse of $F_{IR}=0.5 \text{ J/cm}^2$ its absorption at 1064nm is reduced by 16%, in comparison to the reference/ non irradiated surface. This reduction is due to the selective ablation occurring at the specific wavelength and leads to the attenuation of the PA signal at the 2nd incident laser pulse. In addition, it can be noticed the absorption at 355nm of the surface is increased by 14%. On the other hand, 1p irradiation at 355nm with $F_{UV}=0.5\text{J/cm}^2$ leads to a 16% reduction of the surface absorption in the infrared and 9% in the ultraviolet regime. The differences in the absorption spectra are an indicator of the selective ablation mechanisms and the alteration of the surface material after the interaction with the laser beam. The absorption of all the materials for the wavelengths of 355 and 1064nm are presented in the following table.

Material	Absorption %	
	1064nm	355nm
Crust simulation (G with 5% w/w C)	67	58
Marble	14	22

1p of $F_{IR}=0.50 \text{ J/cm}^2$	56	66
1p of $F_{UV}=0.50 \text{ J/cm}^2$	56	53

Table 10: Absorption before and after single pulse irradiation with $F=0.5 \text{ J/cm}^2$ at 1064 and 355nm.

Furthermore by taking into account that: $T = \frac{\eta_{th}\mu_a F}{\rho C_V}$ it is possible to calculate the ratio of the heat conversion efficiency for the selected wavelengths. The relative temperature ratio has been calculated to be

$$\frac{T_{IR}}{T_{UV}} = 2.051$$

by replacing the measured absorption % for each wavelength we can get that

$$\frac{T_{IR}}{T_{UV}} = \frac{\eta_{th_IR}\mu_{a_IR}}{\eta_{th_UV}\mu_{a_UV}} = \frac{67\% \eta_{th_IR}}{58\% \eta_{th_UV}} \leftrightarrow \frac{\eta_{th_IR}}{\eta_{th_UV}} \sim 1.78.$$

The heat conversion efficiency for the IR wavelength is approximately 1.8 times higher compared to the UV, further confirming that the dominant ablation mechanisms upon irradiation with infrared are photothermal.

Real time Photoacoustic and Optical Monitoring of laser cleaning

The monitoring of the laser cleaning procedure was performed using a time window of $600\mu\text{s}$ and a detection limit of 0.03V , since the background noise was in the order of 0.022V . In order to be able to perform a direct comparison of the photoacoustic amplitude the mean values of the PA signal were normalized to the maximum among them. The irradiation was performed with both wavelengths individually, as well as their simultaneous use. A characteristic example from a measurement performed with individual $F_{IR}=0.5 \text{ J/cm}^2$ and $F_{UV}=0.5\text{J/cm}^2$, and their simultaneous combination with values of $F_{IR}=F_{UV}=0.25 \text{ J/cm}^2$ and $F_{IR}= 0.40 \text{ J/cm}^2$, $F_{UV}=0.10 \text{ J/cm}^2$, is presented below. The simultaneous ratio value of $F_{IR}/F_{UV}=4:1$ was investigated because it was the condition selected as optimum for the cleaning of environmental crusts from marble based in the literature. On the other hand, the $F_{IR}/F_{UV}=1:1$ has been selected as the total fluence value ($F_{IR}+ F_{UV}$) is the same with the total fluence of the optimum cleaning conditions. The spots were irradiated with 20 pulses and, in the selected example presented hereafter, a total number of 27 pairs of spots have been analyzed

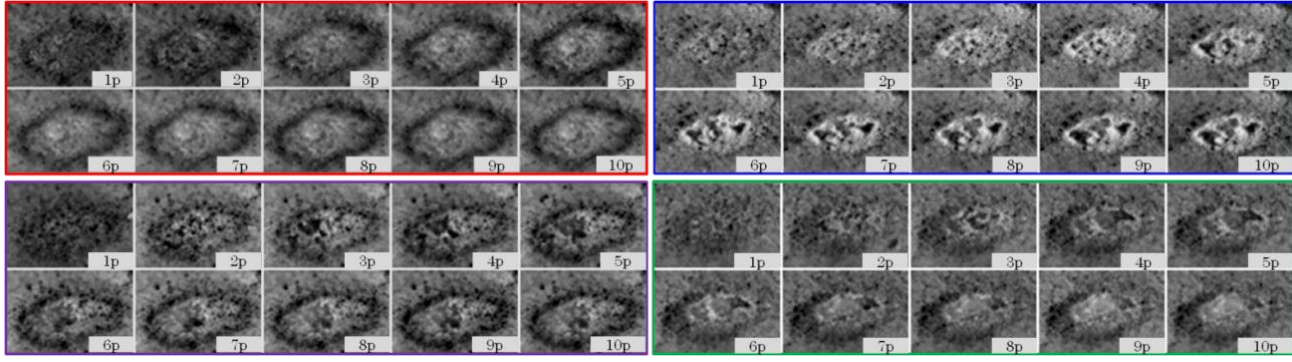


Figure 25: Images recorded for the first 10 incident laser pulses of: $F_{IR}=0.5 \text{ J/cm}^2$ (red frame), $F_{UV}=0.5 \text{ J/cm}^2$ (blue frame), simultaneous $F_{IR}=0.4 \text{ J/cm}^2$ and $F_{UV}=0.1 \text{ J/cm}^2$ (purple frame), simultaneous $F_{IR}=F_{UV}=0.25 \text{ J/cm}^2$ (green frame).

In all cases presented here, the irradiation reveals the marble substrate mainly at the center of the ablated area, where the intensity of the laser beam is higher (Figure 25). The normalized PA signal corresponding to the irradiated spots is presented in Figure 26, and as can be observed, the evolution of the signal presents an exponential decrease. Performing the same robust statistical analysis mentioned earlier the fitting of the data (equation $y= a*x^{-b}$) was characterized by high adjusted R^2 values. During irradiation with the IR and UV laser beams individually with $F=0.5 \text{ J/cm}^2$, the mean PA signal of the 1st incident laser pulse was found to be $\frac{IR}{UV} = 2.05 \pm 0.21$ which is equal to the relative temperature ratio, thus indicating higher temperature rise with the IR beam. The higher temperature rise leads to stronger thermal effects which cause the alteration of the material properties, and specifically its absorption, as can be verified by the $45.5 \% \pm 4.9 \%$ difference among the 1st and 2nd pulse upon 1064nm. On the other hand, 355nm laser ablation leads to a difference of $26.8 \% \pm 5.0 \%$. Simultaneous irradiation with fluence ratio $F_{IR}/F_{UV}=0.4/0.1$ resulted into similar outcome with the IR laser ablation, which can be explained due to the high proportion of the IR laser beam in comparison to the UV. The 1:1 fluence ratio exhibits slightly lower results, indicating that it is less efficient in the material removal in comparison to the 4/1 ratio.

Fitting model $y=a*x^{-b}$	$F_{IR}/F_{UV}=0.4/0.1$	$F_{IR}/F_{UV}=0.25/0.25$
b	0.715 ± 0.091	0.647 ± 0.067
a	0.498 ± 0.072	0.457 ± 0.065
R^2	0.983 ± 0.010	0.987 ± 0.008
1st pulse	0.536 ± 0.053	0.483 ± 0.037
1st – 2nd pulse difference	$43.2 \% \pm 3.1 \%$	$38.4 \% \pm 5.1 \%$

A characteristic example of the normalized PA signal is presented in figure 27 for 20 incident laser pulses. In addition to the decay of the signal, once again we can observe

the plateau that it reached following the 10th pulse. In addition we can observe the variation among the 1st and 2nd pulse of the material for each case.

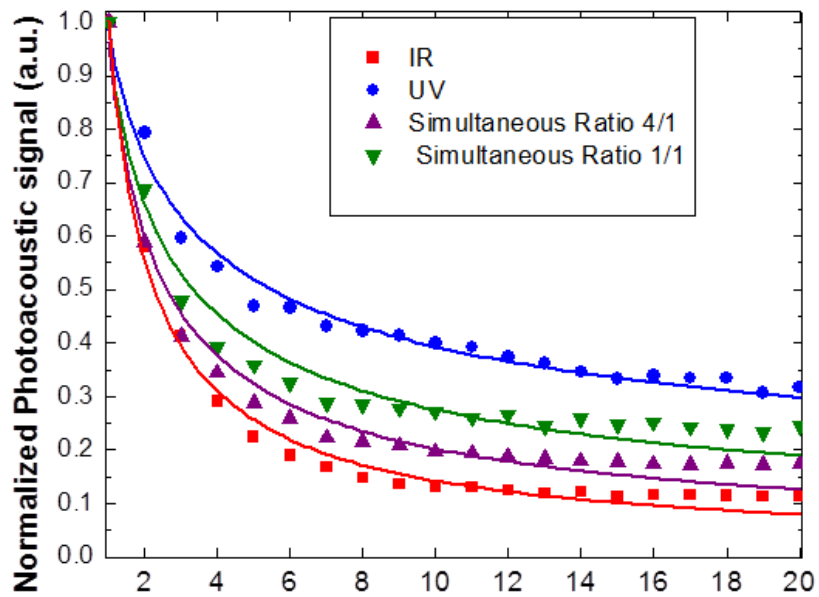


Figure 26: Normalized PA signal for 20 incident laser pulses of: $F_{IR}=0.5 \text{ J/cm}^2$ (red), $F_{UV}=0.5 \text{ J/cm}^2$ (blue), simultaneous $F_{IR}=0.4 \text{ J/cm}^2$ and $F_{UV}=0.1 \text{ J/cm}^2$ (purple), simultaneous $F_{IR}=F_{UV}=0.25 \text{ J/cm}^2$ (green).

Additionally, the absorption spectra of the material after irradiation under these conditions is provided below (figure 27):

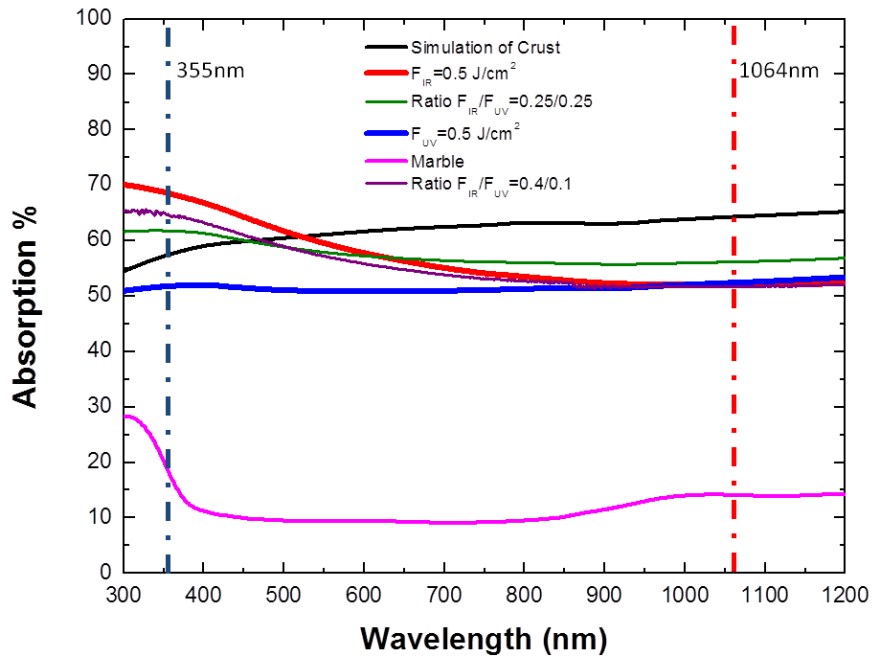


Figure 27: Absorption spectra of the involved materials prior and after irradiation with 1 pulse of selected conditions.

The absorption spectrum confirms the domination of the photothermal mechanisms, similar with IR, for the irradiation with fluence ratio 4/1. In addition, we can observe that the graph corresponding to fluence ratio 1/1 exhibits a different response, indicating the different ablation mechanisms that occur under those conditions.

Although the evolution of the ablation process could be monitored, a separation among the end of the ablation process due to laser induced changes to the material properties and the complete removal of the encrustation layer, was not possible in this low fluence regime. For example, we can see below two different spots of the same sample irradiated with $F_{IR}=0.5 \text{ J/cm}^2$ and 20 pulses. In the first case the ablation of the material/crust has ended due to laser induced modifications while in the second the crust is removed completely.

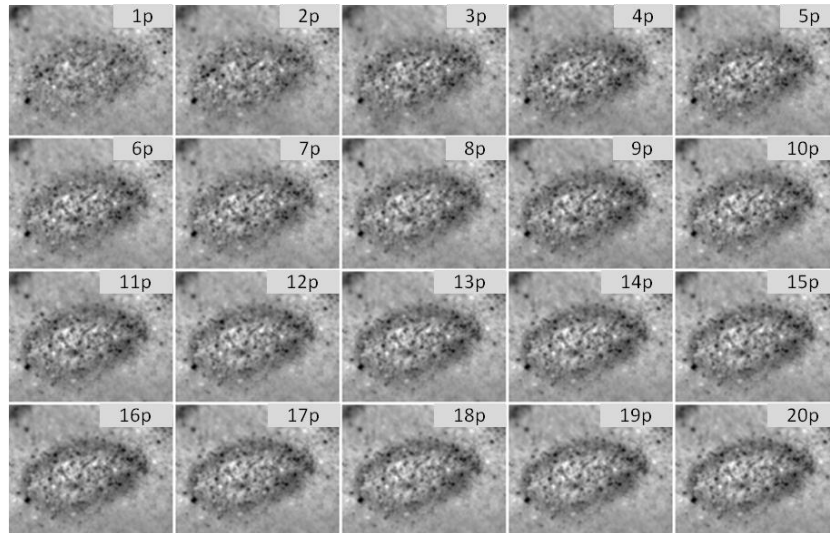


Figure 28: Optical images recorded for a series of consecutive pulses on the same spot for a case that the crust is not effectively removed. The irradiation was performed with $FIR=0.5 \text{ J/cm}^2$.

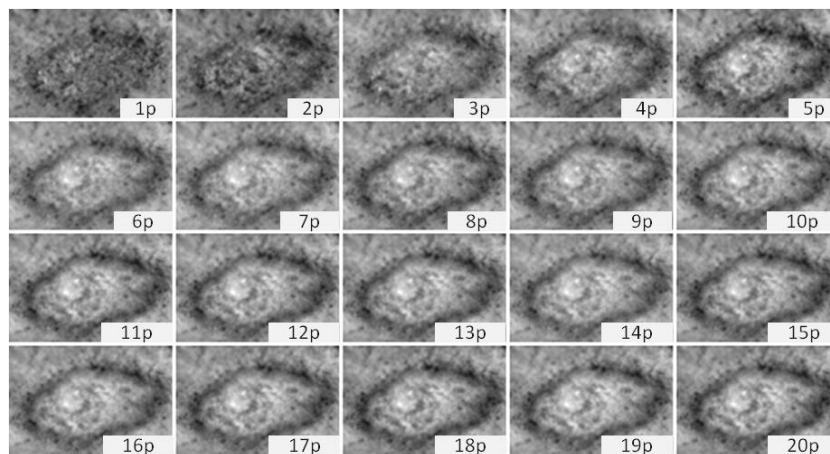


Figure 29: Optical images recorded for a series of consecutive pulses on the same spot for a case that the crust is removed. The irradiation was performed with $FIR=0.5 \text{ J/cm}^2$.

Although through the recorded images the two different cases can be distinguished, the normalized PA signal exhibits a similar trend, in both cases, as can be observed in figure 30:

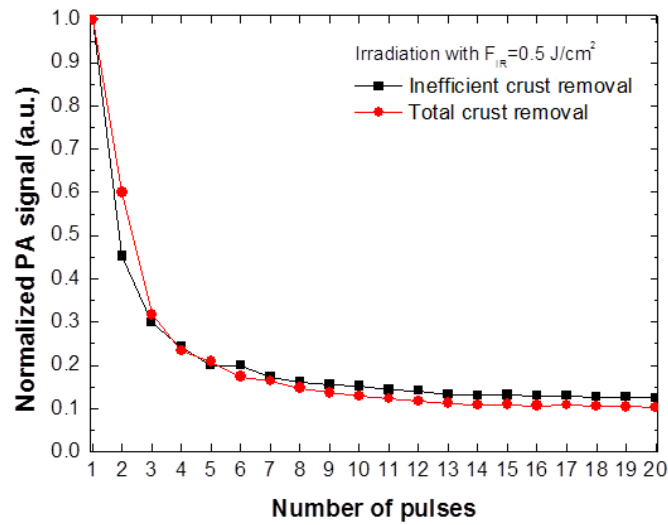
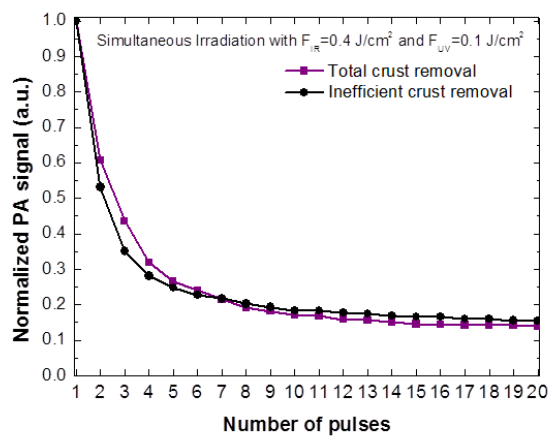
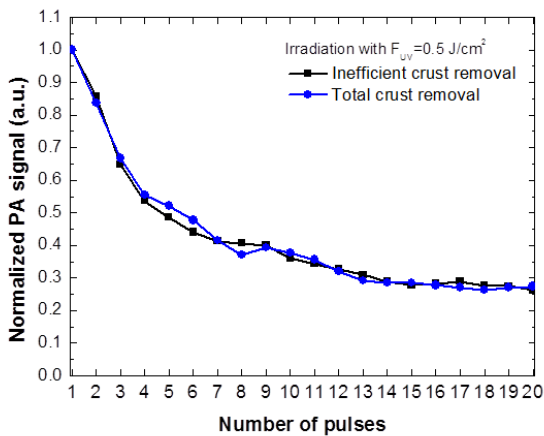


Figure 30: Example of irradiation with $F_{IR}=0.5 \text{ J/cm}^2$. The evolution of the normalized PA signal is presented for a spot with total crust removal (red line) and a spot with insufficient crust removal the removal is not achieved (black line).

The same problem was encountered with the UV wavelength, as well as, their simultaneous combination in different fluence values. Characteristic examples from each case, irradiation with $F_{UV}=0.5 \text{ J/cm}^2$, simultaneous $F_{IR}=F_{UV}=0.25 \text{ J/cm}^2$, simultaneous $F_{IR}= 0.40 \text{ J/cm}^2$ $F_{UV}=0.10 \text{ J/cm}^2$, are presented below.



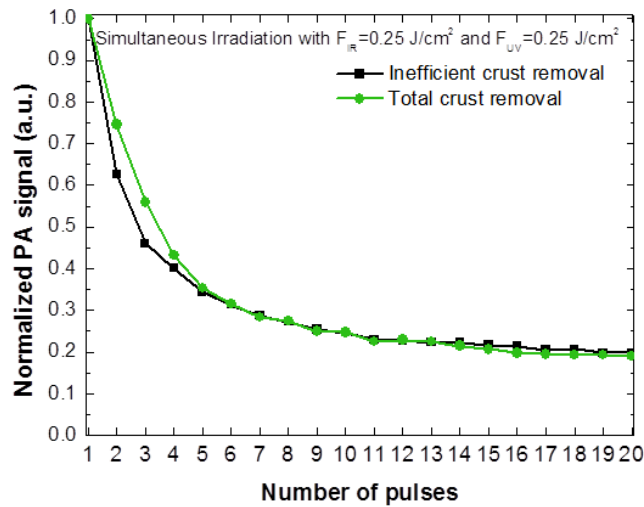


Figure 31: Examples of the evolution of the normalized PA signal for different irradiation Conditions. In all graphs the black line represents the evolution of the PA signal when the crust is not removed. The normalized the normalized PA signal process for effective cleaning is noted with color. Specifically, the top left graph corresponds to $F_{UV}=0.5 \text{ J/cm}^2$ (blue), the top right to simultaneous $F_{IR}=0.4 \text{ J/cm}^2$ and $F_{UV}=0.1 \text{ J/cm}^2$ (purple), and the bottom on simultaneous $F_{IR}=F_{UV}=0.25 \text{ J/cm}^2$ (green).

Therefore, a different approach was required in order to be able to distinguish the complete material removal using only the PA signal in this low Fluence regime. The process could of course be monitored through the recorded optical images, yet other possibilities and prost process protocols needed to be considered regarding the PA signal.

Cross Correlation photoacoustic signal analysis

Implementation of Cross Correlation for the Monitoring of laser cleaning

In order to further optimize the monitoring process and obtain accurate information regarding the cleaning efficiency through the PA signal, we investigated the possibility to obtain more information from the recorded waveform. To achieve this, the sampling resolution of the waveform needed to be increased, in order to distinguish the unique characteristics of the intrinsically generated PA signal. Therefore, the recording temporal window was decreased to $60 \mu\text{s}$ instead of the initial $600\mu\text{s}$ that was used, while the sampling points remained 1.000. Afterwards, different post processing analysis of the data was considered to establish a protocol that could actually detect the incident laser pulse that removes the crust, revealing the marble substrate.

To achieve this, a cross correlation (CC) operation between the PA waveforms generated at each incident pulse ($N=2,3,4\dots$) and the first pulse ($N=1$) was considered. The cross correlation is a common signal processing method which measures the similarity of two waveforms $f(t)$ and $g(t)$ as a function of the time

displacement to one relative to the other. This is also known as the sliding dot product or sliding inner product and is defined as:

:

$$(f * g)(\tau) = \int_{-\infty}^{\infty} f^*(t)g(t + \tau)dt$$

where f^* denotes the complex conjugate of f , and τ is the temporal displacement

One can use the cross-correlation to find how much g must be shifted along the time-axis to make it identical to f . The formula essentially slides the g function along the time axis, calculating the integral of their product at each position. When the functions match, the value of (f^*g) is maximized.

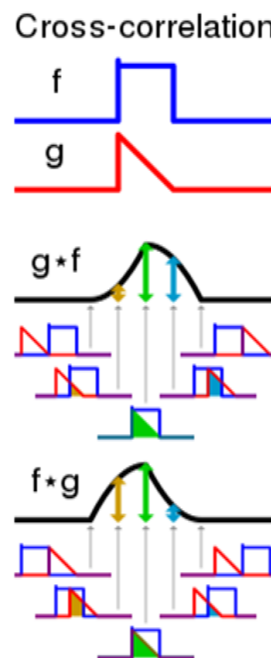


Figure 32: Visual explanation of the Cross Correlation between two functions f and g

As mentioned previously, PA waveforms generated by each laser pulse were initially cross correlated with the respective waveform resulting from the first one. Subsequently, the maximum amplitude of the cross correlation product was extracted and analyzed. Using the absolute value of the percentage change in the maximum amplitude of the cross correlation operation, it was possible to determine the incident laser pulse for which the unwanted material was removed from the sample. Below we can see a characteristic example of the cross correlation results for a spot irradiated with $F_{IR}=0.8 \text{ J/cm}^2$ and a total of 20 pulses (figures 33 and 34).

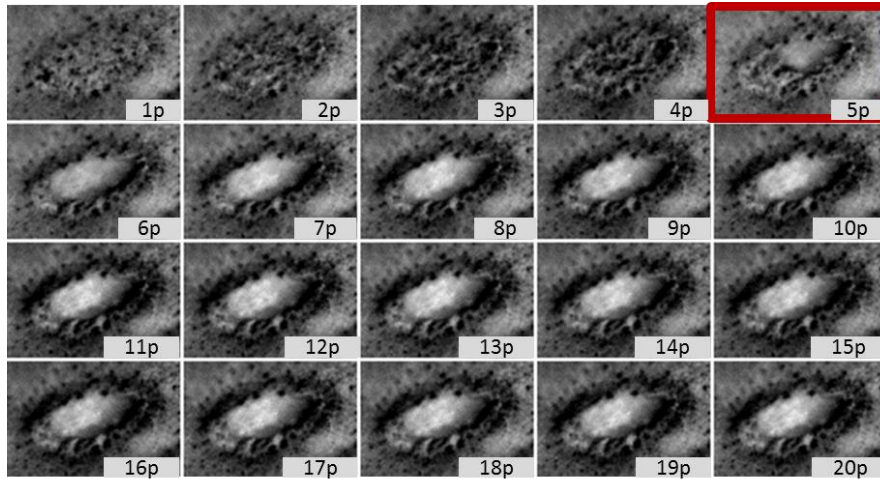


Figure 33: Optical images of 20 incident laser pulses with $F_{IR}=0.8 \text{ J/cm}^2$

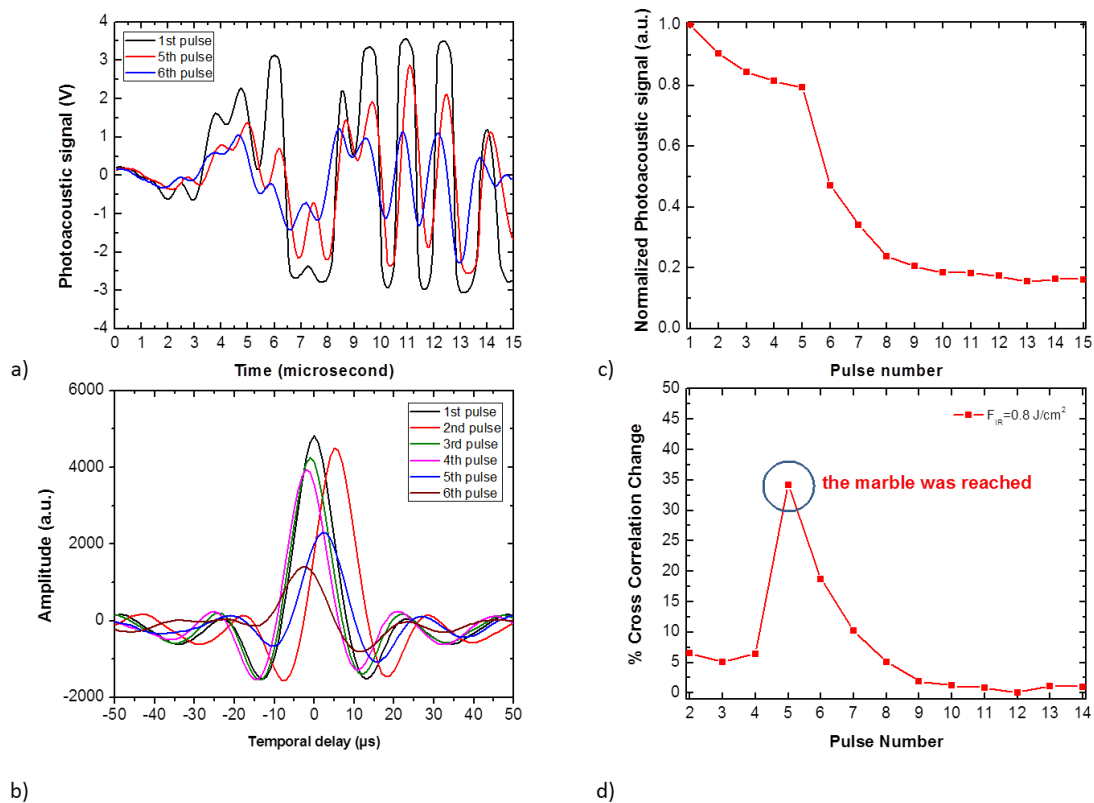


Figure 34: a) Recorded PA waveform for $F_{IR}=0.8 \text{ J/cm}^2$, b) Cross Correlation with the waveform recorded from the first pulse, c) Maximum amplitude of Cross Correlation for the first 15 laser pulses, d) % of Cross Correlation maximum amplitude change

From Figure 33, we can observe that the crust has been removed after the 5th laser pulse, while the thickness of the removed material at the end of the irradiation process was $104.6 \pm 29.8 \text{ } \mu\text{m}$, as measured by profilometry. The evolution of the amplitude of the cross correlation can be observed at Figure 34 c) and d). It can be seen that the pulse that completely removes the crust, in the maximum amplitude graph, it is not clearly distinguishable. However, the percentage change of the Cross

Correlation maximum amplitude presents a clear and easily detected peak at the pulse that eliminates the unwanted material. Following this approach, we were also able to distinguish among 3 different cases where a) crust could not be removed totally b) the depositions were efficiently removed and c) the substrate was damaged due to high fluence values above substrate's threshold. Some representative examples are presented in Figure 35. The irradiation was performed with fluence values $F=1.0 \text{ J/cm}^2$, $F=0.8 \text{ J/cm}^2$ and $F=0.6 \text{ J/cm}^2$. In general, using the IR wavelength, characteristic peaks with values above 20 % are detected when the over layer is removed.

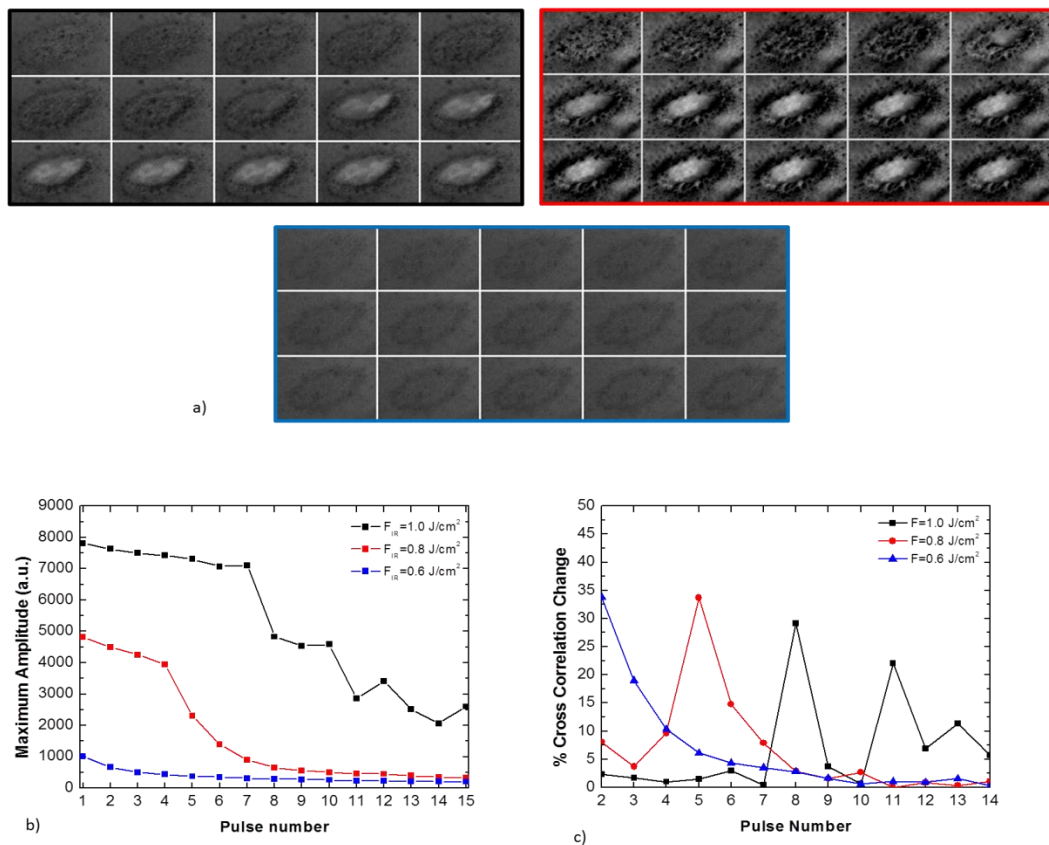


Figure 35: a) Recorded optical images for the investigated Fluence values, with black frame $F=1.0 \text{ J/cm}^2$, red frame $F=0.8 \text{ J/cm}^2$ and with blue frame $F=0.6 \text{ J/cm}^2$. b) Cross Correlation maximum amplitude and c) the CC maximum amplitude % change for different fluence values. Blue low F (unsuccessful crust removal), Red optimum F (efficient removal without damage), Black high F (removal of crust with damage on the substrate)

In black color, we can observe a spot irradiated with $F=1.0 \text{ J/cm}^2$; this fluence value exceeds the ablation threshold of the substrate and induces damage to the marble. The crust is removed at the 8th pulse as can be additionally detected from the optical images (Figure 35 a) and also from the peak of Figure 35 c. The additional peaks seen at Figure 35c correspond to the ablation of the marble and the further extraction of material, the crater created has a depth of approximately $163.2 \pm 32 \mu\text{m}$ as measured by profilometry. The irradiation condition of $F=0.8 \text{ J/cm}^2$ is highlighted with red color in Figure 35c. This is the optimum irradiation condition in this case, as it effectively removes the crust layer while leaving the substrate intact. The unwanted layer is

eliminated at the 5th laser pulse as observed from the optical images and the graph in Figure 35c. Further ablation of the sample does not result in material removal from the marble or grain extraction, confirmed also by the absence of peaks after the 5th pulse at Fig. 35c. The irradiation condition that corresponds to a low fluence value ($F=0.6 \text{ J/cm}^2$) incapable of removing the crust (Figure 35) is denoted with blue color in Figure 35d. The crater depth is not significant in this case (approximately $55.3 \pm 10.5 \mu\text{m}$) while the absence of peaks in graph of figure 35c confirms the ineffective ablation.

The same study was carried out for the wavelength of 355nm. A representative example is provided below for the fluence value of $F=0.5 \text{ J/cm}^2$ for a spot where the marble is reached at the 3rd laser pulse.

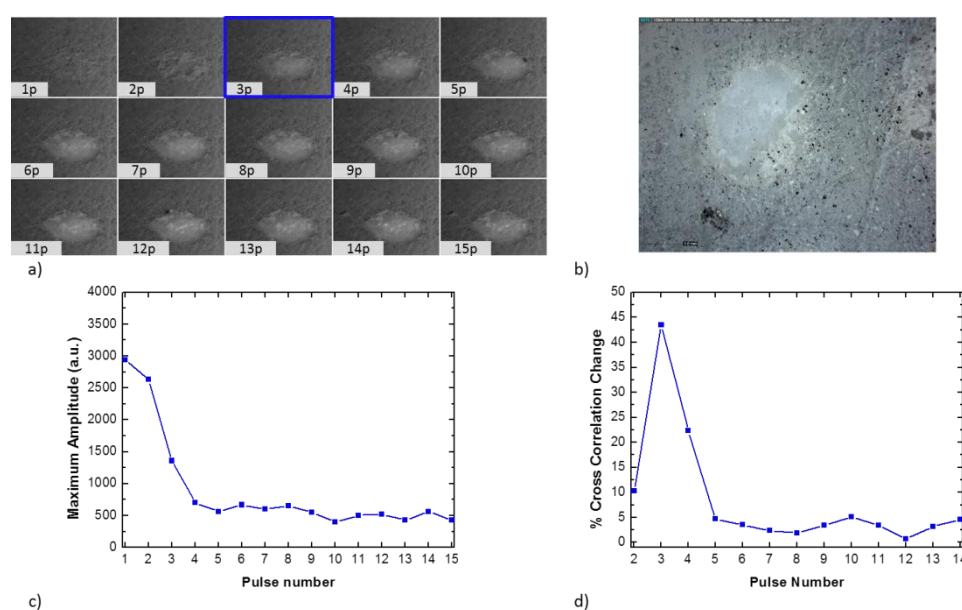


Figure 36: a) the recorded optical image after every laser pulse is presented b) on microscopic photo of the irradiated spot. c and d) Example of Cross Correlation for irradiation with $F=0.5 \text{ J/cm}^2$ at 355nm. The crust is removed at the 3rd laser pulse.

The material is eliminated in the 3rd laser pulse as seen from figure 36a and detected from the peak at figure 36d. In figure 36 b a photograph of the spot under optical microscope is presented after the irradiation. The microscopic image reveals signs of micro-damage of the marble, while the depth of the ablated spot corresponds to approximately $113.8 \pm 22.4 \mu\text{m}$. In order to confirm the substrate damage, further process of the optical images recorded from the monitoring system was implemented.

This approach allows to enhance features of the recorded optical images and subsequently extract information regarding interaction of the laser beam with the marble were extracted. The images were processed with ImageJ program. Below (Figure 37), subtracted image of the 1st and 3rd incident pulse and the 3rd and 15th pulse for the example of figure 36 are explicitly presented. For each selected pair, the images were subtracted (i.e. image of 1st pulse from 3rd, and 3rd from 1st) and the two

resulted images were added, eliminating noise effects and enhancing features (due to variations in the pixel intensity) previously not easily detected.

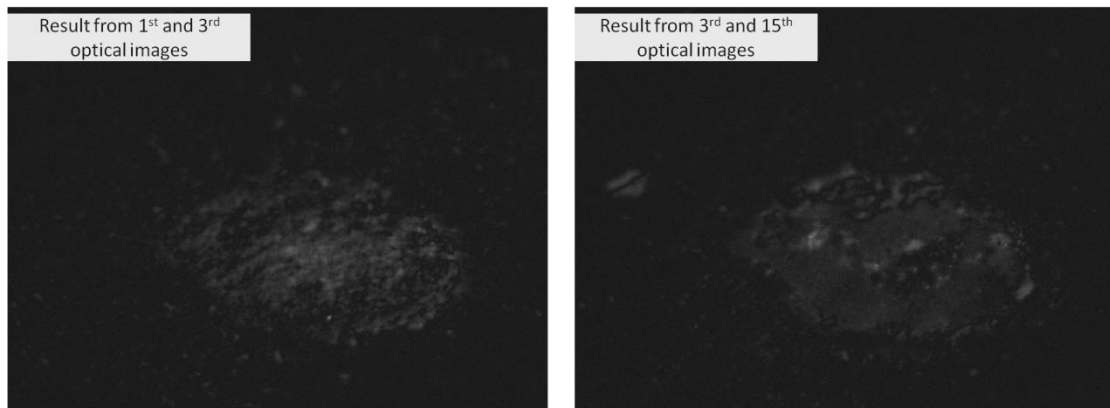


Figure 37: Final images after the process. Left image corresponds to the result from the image process of the 1st and 3rd laser pulse. Right image corresponds to the process image of the 3rd and 15th laser pulse.

The images were selected on the basis that the material is removed between the 3rd and 1st incident laser pulse, and that from the 3rd pulse and after the laser beam interacts only with the marble substrate. Regarding the final images, the one corresponding to the result of the 1st and 3rd pulse we can observe the material removal. The image produced from the process of the 3rd and 15th laser pulse confirms the further removal of material. An easily detected spot is observed, indicating that micro damage to the surface has been induced.

It has to be mentioned that for higher fluence values at 355nm the percentage change of the Cross Correlation maximum amplitude did not provide clear results. This can be attributed to the intense ablation phenomena and the high material removal rate, which reduces the similarity of the generated waveforms. Below, we present an example of irradiation with $F=1.0 \text{ J/cm}^2$ at 355nm (figure 38). The cleaning progress cannot be monitored, while the thickness of the ablated material reaches approximately the 1mm.

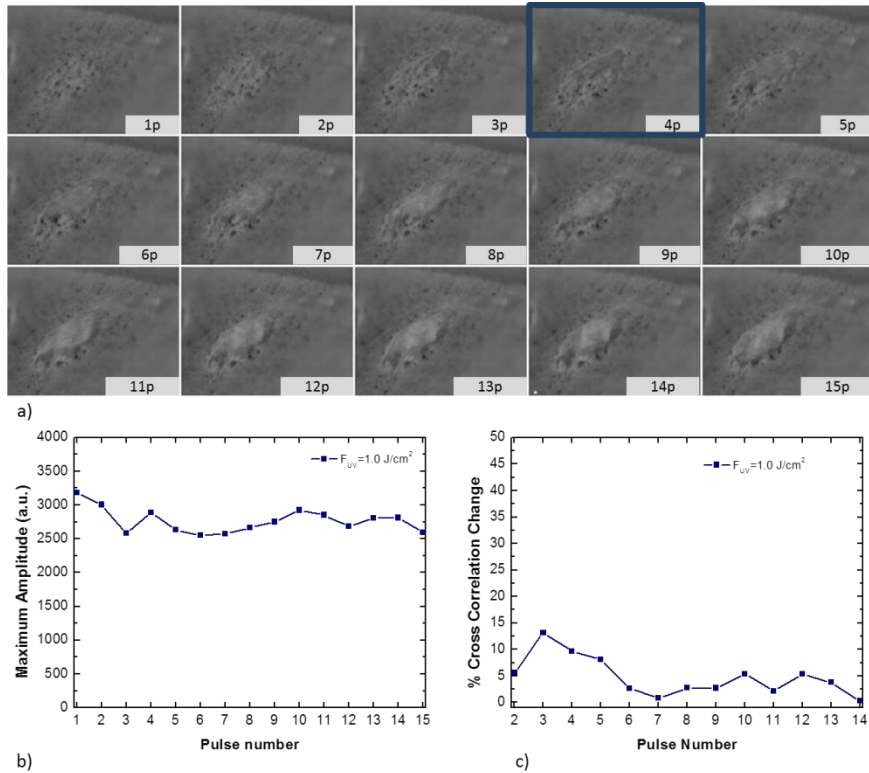


Figure 38: Result from irradiation with $F=1.0 \text{ J/cm}^2$ at 355nm. The irradiation condition exceeds the marble's ablation threshold. The evolution of the irradiation process cannot be monitored in this case.

The same methodology was followed for the simultaneous use of both wavelengths in a variety of fluence ratio values. The examined irradiation conditions are $F_{IR}/F_{UV}=0.8/0.2$, $F_{IR}/F_{UV}=0.8/0.2$, $F_{IR}/F_{UV}=0.5/0.5$, $F_{IR}/F_{UV}=0.25/0.25$. The fluence values were selected initially in order to have a total fluence of 0.5 J/cm^2 , but with this condition it was not easy to completely remove the crust. Therefore, the total fluence value was increased at 1.0 J/cm^2 so to have enough energy for the effective ablation of the material. Selected examples from the results are presented below.

Ratio 1 / 1

Starting from the lowest fluence values tested for the equal contribution ratio $F_{IR}/F_{UV}=0.25/0.25$, we can observe that the energy of the laser beam is not enough to remove the unwanted material. In figure 39 (a) we can see the evolution of the ablation progress through the first 15 incident pulses, while in figure 39 b a microscopic image recorded after the irradiation process can be observed. The irradiated spot has been discolored, yet a crater with significant depth cannot be discriminated. As measured by profilometry only approximately $34.5 \pm 11.2 \mu\text{m}$ of material have been removed.

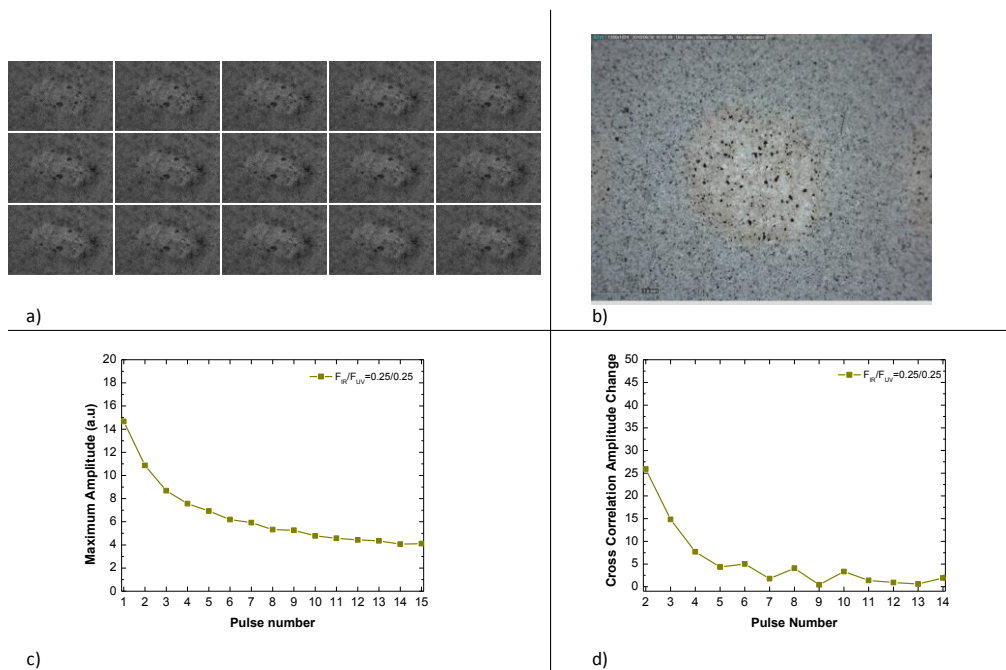


Figure 39: a) Optical images from irradiation with $F_{IR}/F_{UV}=0.25/0.25$ for 15 incident laser pulses; b) microscopic image of the spot after the irradiation where only discoloration of the material is observed; c) maximum amplitude of Cross Correlation; d) Percentage difference of maximum amplitude of Cross Correlation with the 1st pulse.

The amplitude of the Cross Correlation is lower in comparison with the previous examples presented, as expected due to the low irradiation energy. In addition, the subtracted images do not present any signs of material extraction. The following image is the result of subtraction and addition of images 1 and 15 from the above example.



Figure 40: Result of subtraction and addition of images 1 and 15 for irradiation with $F_{IR}/F_{UV}=0.25/0.25$ where only discoloration phenomena are observed.

For $F_{IR}/F_{UV}=0.5/0.5$ the unwanted material removal was achieved but damage to the marble substrate occurred. In Figure 41, a characteristic example of irradiation under this condition is presented. The deposition layer is removed at the 5th -6th laser pulse, but additional pulses induce damage to the marble, easily detected also through the microscopic image Figure 41 b.

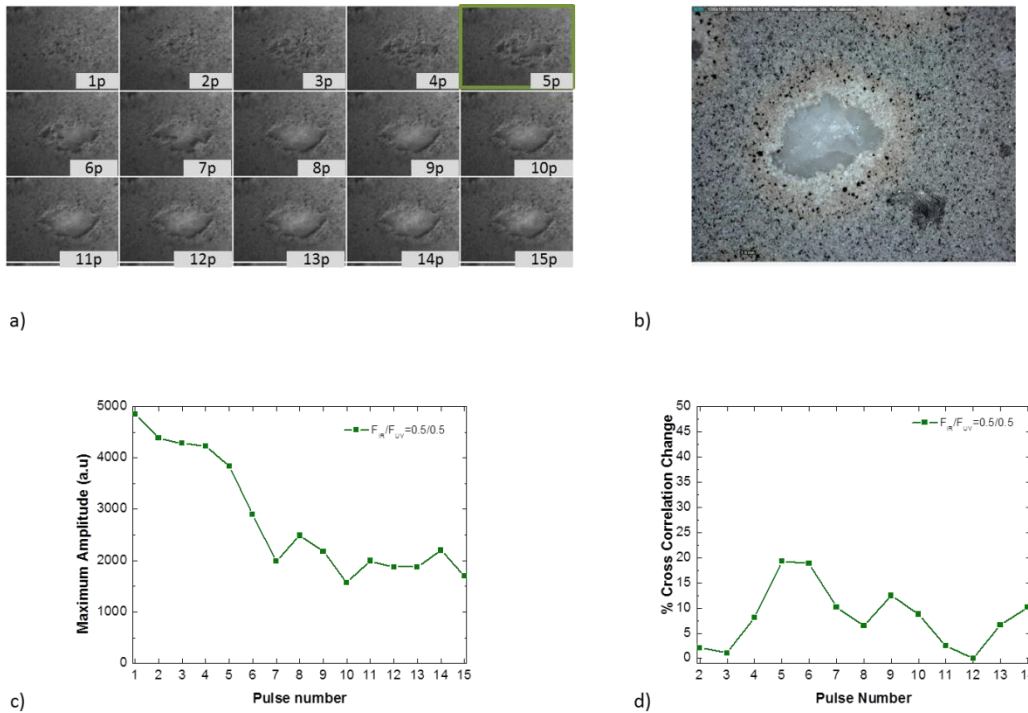


Figure 41: a) Optical images from irradiation with $F_{IR}/F_{UV}=0.5/0.5$ for 15 incident laser pulses; b) microscopic image of the spot after the irradiation where damage to the marble is observed; c) maximum amplitude of Cross Correlation; d) Percentage difference of maximum amplitude of Cross Correlation with the 1st pulse. The crust is removed at the 6th laser pulse (first peak) while further pulses induce damage to the marble (2nd peak).

Even though this condition exceeded the marbles ablation threshold, confirmed also by the subtraction and addition of images in Figure 42, the cleaning progress could be monitored. The detected peaks present lower percentage values in comparison to the ones detected when only the IR wavelength was involved, possibly due to the high contribution of the UV beam.

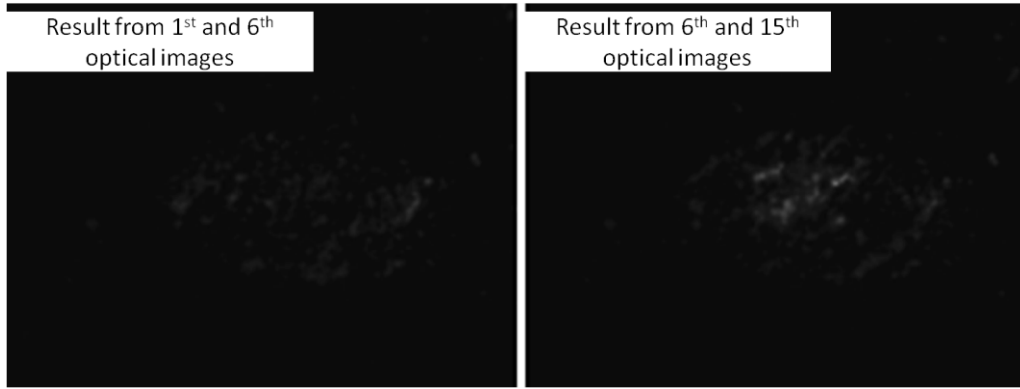


Figure 42: Result from the subtraction and addition of images corresponding to the 1st and 6th pulse (left) and the 6th and 15th pulse (right), with $F_{IR}/F_{UV}=0.5/0.5$. The latter indicates the damage induced to the marble.

Ratio 4 / 1

This fluence ratio was investigated as it has been proved, in literature[6], to effectively remove the crust and at the same time confront the laser induced discoloration. Initially a total fluence value of 0.5 J/cm^2 was used, in specific $F_{IR}/F_{UV}=0.4/0.1$. A representative example is presented below (figure 43).

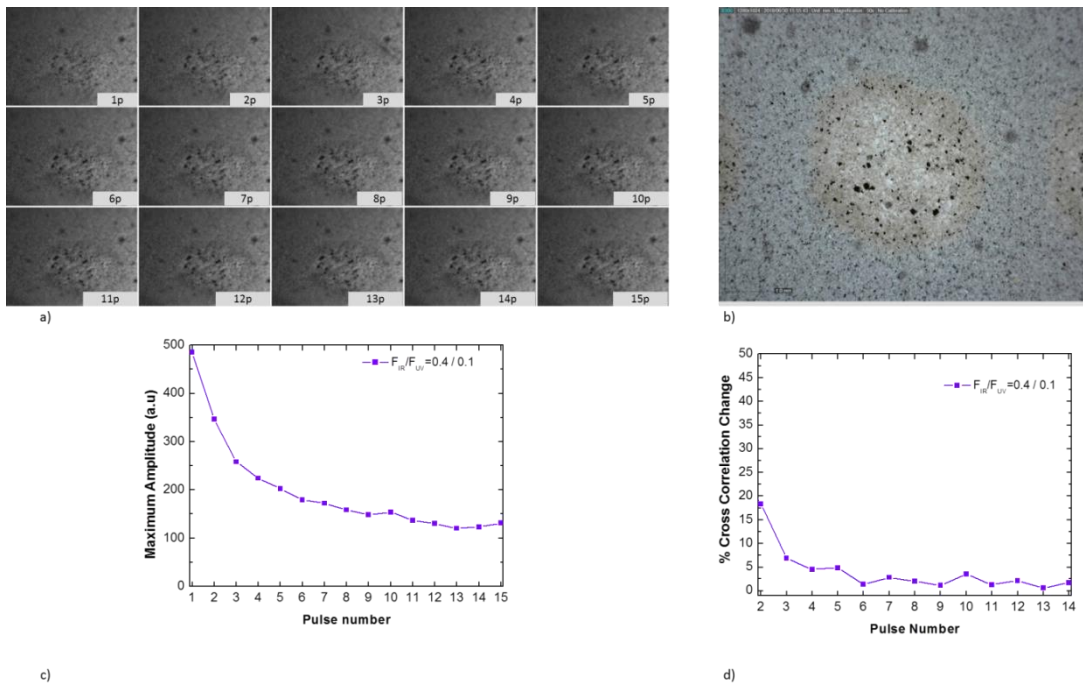


Figure 43: a) Optical images from irradiation with $F_{IR}/F_{UV}=0.4/0.1$ for 15 incident laser pulses; b) microscopic image of the spot after the irradiation only discoloration of the material is observed; c) maximum amplitude of Cross Correlation; d) Cross Correlation amplitude change.

The total energy density could induce only discoloration to the crust, with minimal material extraction. The maximum amplitude of the Cross Correlation with the 1st pulse presents again low values, as in the 0.25/0.25. The decay of the cross correlation of the amplitude change indicates the inefficient material removal.

For $F_{IR}/F_{UV}=0.8/0.2$ the crust was effectively removed from the substrate at the 4th incident laser pulse, as confirmed by optical images and the cross correlation amplitude change (Figure 44 a and d). The thickness of the removed material after 15 laser pulses was measured to be $154.4 \pm 51.5 \mu\text{m}$, while the second peak observed at the 8th pulse from figure 43 d indicates possible damage of the substrate.

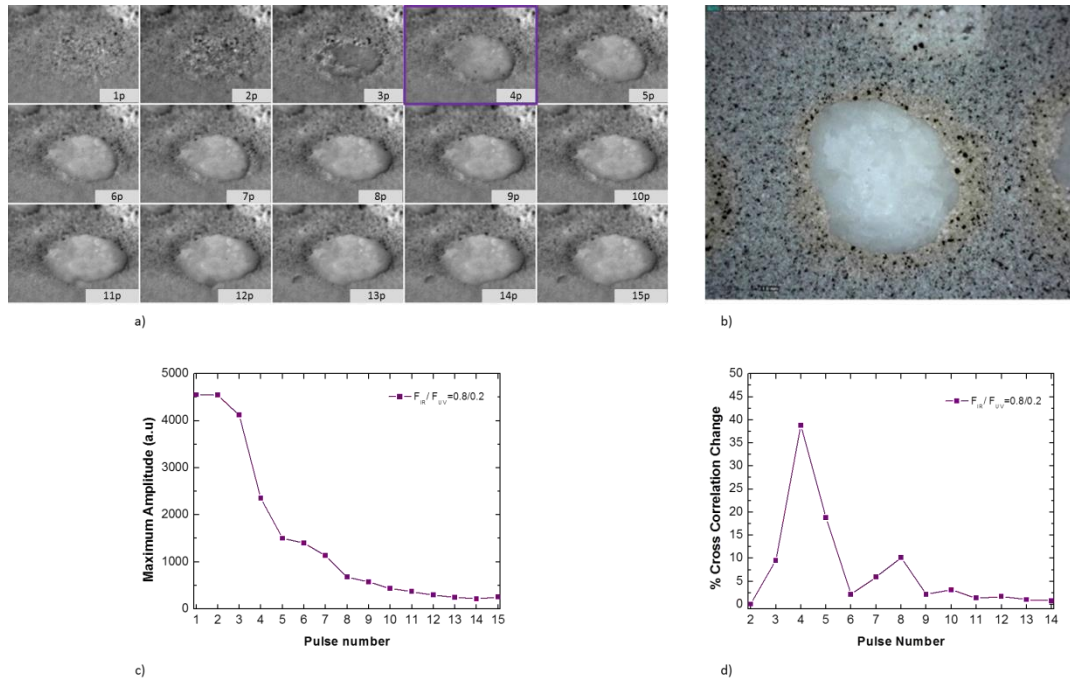


Figure 44: a) Optical images from irradiation with $F_{IR}/F_{UV}=0.8/0.2$ for 15 incident laser pulses; b) microscopic image of the spot after the irradiation where the material is removed; c) maximum amplitude of Cross Correlation; d) Cross Correlation amplitude change, indicating the material removal and possible damage to the marble.

The further removal of material after the elimination of the crust can be confirmed by the processed images (figure 45).

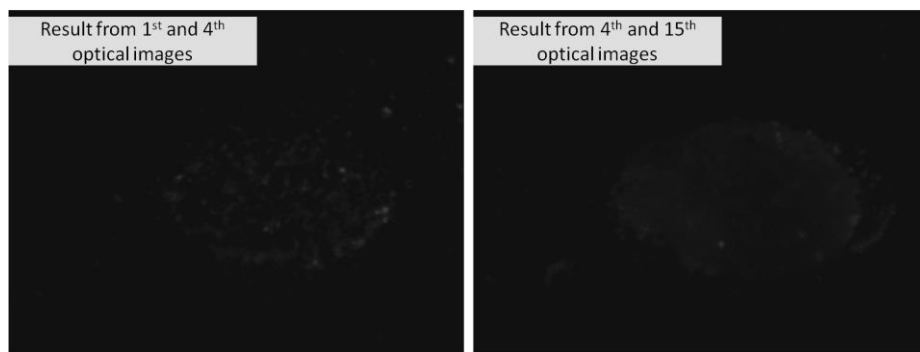
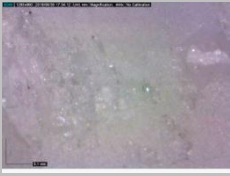
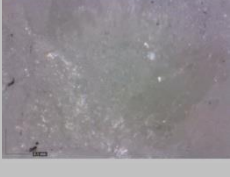


Figure 45: Result of subtraction and addition of images 1 and 4 (right) and 4 and 15 (left) for irradiation with $F_{IR}/F_{UV}=0.8/0.2$. The right image confirms the damage of the substrate.

Evaluation of ablation thresholds with Cross Correlation analysis

The cross correlation methodology was implemented for the investigation of the possible damage of the marble regarding the irradiation conditions presented in the previous paragraph. The assessment of the results was performed using optical

microscopy and profilometry as additional evaluation methods. The results are summarized in the following table.

Irradiation Condition (J/cm²)	Number of pulses	Damage	Crater Depth (profilometry, μm)	Optical Microscopy (after 20 pulses)
F_{IR}=0.8	20 and 72	No (20p) and yes (72p)	Zero (20p) and 64.15±9.56 (72p)	
F_{IR}=0.5	20	Not detected	Zero	
F_{IR}=0.4	20	Not detected	Zero	
F_{UV}=0.5	20	yes	46.73±15.35	
F_{UV}=0.2	20	Not detected	Zero	
F_{UV}=0.1	20	Not detected	Zero	
F_{IR}/F_{UV}=0.8/0.2	20	yes	37.33±12.6	

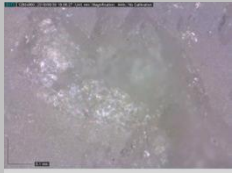
$F_{IR}/F_{UV}=0.4/0.1$	20	Not detected	Zero	
$F_{IR}/F_{UV}=0.5/0.5$	20	yes	173.9 ± 9.35	
$F_{IR}/F_{UV}=0.25/0.25$	20	Not detected	Zero	

Table 11: Fluence values tested on marble and evaluated with profilometry and microscopic images.

The corresponding photoacoustic results for the irradiation conditions that the generated PA signal was above the detection limit of the system are shown below:

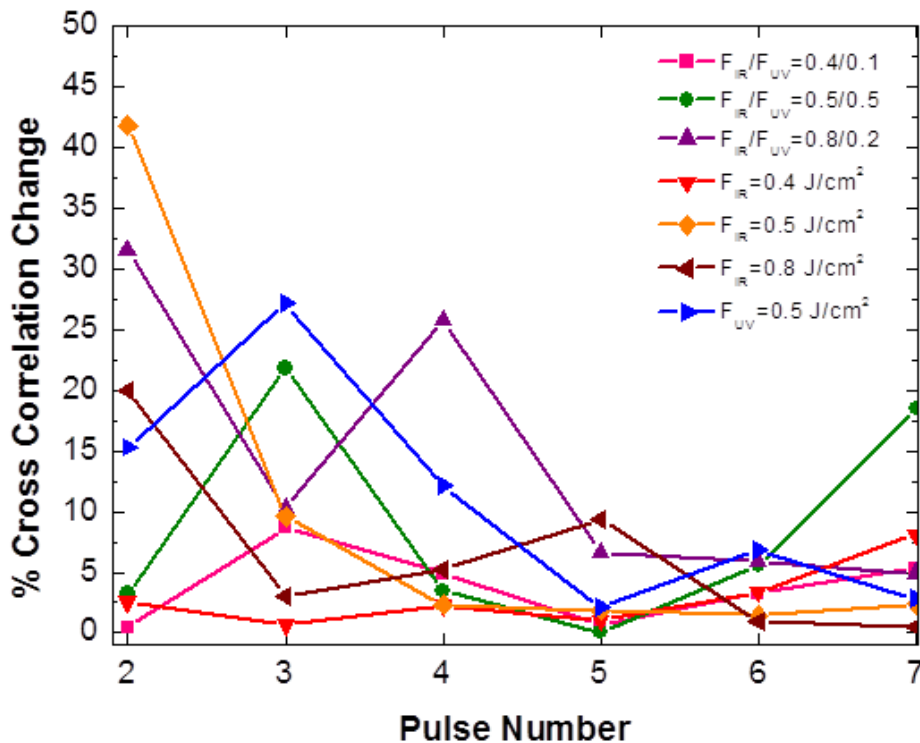


Figure 46: Difference in Cross Correlation amplitude from irradiation of marble under different conditions.

The conditions that correspond to $F_{IR}/F_{UV}=0.8/0.2$, $F_{IR}/F_{UV}=0.5/0.5$ and $F_{UV} = 0.5 \text{ J/cm}^2$ present a peak above 20% indicating the damage induced to the marble; as has also been confirmed through the Optical microscope and the profilometer. Irradiation

condition with $F_{IR} = 0.8 \text{ J/cm}^2$ and $F_{IR} = 0.5 \text{ J/cm}^2$ present a maximum at the 1st irradiation pulse which drops below 10% at the second pulse. This behavior can be attributed to the removal of some superficial deposition, possible due to some dust/dirt on the sample surface, without further ablation or grain extraction. The fluence values of $F_{IR} = 0.4 \text{ J/cm}^2$ and $F_{IR} / F_{UV} = 0.4/0.1$ cannot be associated with any damage effects as can be observed from figure 46, and confirmed through microscopic examination and profile measurements. The rest of the irradiation conditions could not provide accurate results because the intrinsically generated photoacoustic signal exhibited values close to the detection limit of the system.

Conclusions and Future Research

In summary, we have developed a hybrid photoacoustic and optical system for the monitoring of laser cleaning and the investigation of the laser ablation mechanisms that dominate the cleaning at IR and UV laser wavelengths. Until now, a compact set up dedicated to those purposes had not been developed, while the application of the photoacoustic technique for the elucidation of the laser cleaning mechanisms has been considered for the first time. So far, we have demonstrated the potential of the system for the monitoring of laser cleaning with IR and UV wavelengths, both individually and simultaneously in a variety of fluence values. We compared the generated PA signal from the two different wavelengths and associated it with the laser ablation mechanisms, confirming the models supporting the domination of photothermal mechanisms during IR irradiation. In addition, we calculated the ratio of the relative temperatures that are induced upon IR and UV laser ablation, which for our studies on simulated pollution crust was calculated to be $T_{IR}/T_{UV} \sim 2$. Furthermore, we introduced a novel photoacoustic data processing protocol which can be used to indicate the incident pulse that eliminates the crust layer, using only the generated waveform from the interaction of the laser beam with the material. Finally, using the same approach, we evaluated the ablation thresholds of the marble for selected irradiation conditions, showing the accuracy offered by the Photoacoustic technique.

This prototype system can be used for the monitoring of the laser cleaning in real cases. In fact, some preliminary results from stone fragments exposed to urban environments are promising. In the future we are planning to integrate non – contact transducers in the monitoring experimental setup, which will increase the system portability and will allow the accurate implementation of the technique in samples with variable surface geometries. The use of such detectors can also allow the monitoring of cleaning procedures in objects with fragile and delicate surfaces, where non-contact monitoring methodologies are required. In addition, developments in the software are planned to be performed in order to monitor the cleaning progress of larger areas, either during a cleaning process that is performed using an automated procedure or for interventions performed by a conservator. In the case of an automated cleaning procedure, the maximum Cross Correlation amplitude change can be employed to regulate the incident number of laser pulses released on the sample based on the local thickness of the crust and the irregularities of the surface morphology.

A systematic study of a wider variety of materials and combination of substrates with deposition layers can result in the creation of a database regarding the onsets of damage as well as effective and ineffective cleaning conditions. In this manner, the system could be easily adjusted to monitor automatically the cleaning interventions in a variety of materials.

References

1. Asmus, J.E., *More light for art conservation*. IEEE Circuits and Devices Magazine, 1986. **2**(2): p. 6-15.
2. Fotakis C., D.A., V. Zafirooulos, S. Georgiou, V. Tornari, *Lasers in the Preservation of Cultural Heritage; Principles and applications*. 2006, New York: Taylor and Francis
3. Cooper, M.I., D.C. Emmony, and J. Larson, *Characterization of laser cleaning of limestone*. Optics & Laser Technology, 1995. **27**(1): p. 69-73.
4. Cooper, M.I., *Laser Cleaning in Conservation: An Introduction*. 1998, Oxford: Butterworth Heinemann.
5. Pouli, P., M. Oujja, and M. Castillejo, *Practical issues in laser cleaning of stone and painted artefacts: optimisation procedures and side effects*. Applied Physics A, 2012. **106**(2): p. 447-464.
6. Pouli, P., et al., *The two-wavelength laser cleaning methodology; theoretical background and examples from its application on CH objects and monuments with emphasis to the Athens Acropolis sculptures*. Heritage Science, 2016. **4**(1): p. 9.
7. Melessanaki, K., et al., *Laser Cleaning and Spectroscopy: A Synergistic Approach in the Conservation of a Modern Painting*. Laser Chemistry, 2006. **2006**: p. 1-5.
8. Salimbeni, R., R. Pini, and S. Siano, *Achievement of optimum laser cleaning in the restoration of artworks: expected improvements by on-line optical diagnostics*. Spectrochimica Acta Part B: Atomic Spectroscopy, 2001. **56**(6): p. 877-885.
9. Fortes, F.J., L.M. Cabalín, and J.J. Laserna, *The potential of laser-induced breakdown spectrometry for real time monitoring the laser cleaning of archaeometallurgical objects*. Spectrochimica Acta Part B: Atomic Spectroscopy, 2008. **63**(10): p. 1191-1197.
10. Maravelaki, P.V., et al., *Laser-induced breakdown spectroscopy as a diagnostic technique for the laser cleaning of marble*. Spectrochimica Acta Part B: Atomic Spectroscopy, 1997. **52**(1): p. 41-53.
11. Papadakis, V., A. Loukaiti, and P. Pouli, *A spectral imaging methodology for determining on-line the optimum cleaning level of stonework*. Journal of Cultural Heritage, 2010. **11**(3): p. 325-328.
12. Pozo-Antonio, J.S., et al., *Hyperspectral Imaging as a Non Destructive Technique to Control the Laser Cleaning of Graffiti on Granite*. Journal of Nondestructive Evaluation, 2016. **35**(3): p. 44.
13. Bernikola, E., et al., *Real-time monitoring of laser-assisted removal of shellac from wooden artefacts using digital holographic speckle pattern interferometry*. 2013. 52-58.
14. Taruttis, A. and V. Ntziachristos, *Advances in real-time multispectral optoacoustic imaging and its applications*. Nature Photonics, 2015. **9**: p. 219.
15. Tam, A.C., *Applications of photoacoustic sensing techniques*. Reviews of Modern Physics, 1986. **58**(2): p. 381-431.
16. Rosencwaig, A., *Photoacoustics and photoacoustic spectroscopy / Allan Rosencwaig*. Chemical analysis ; v. 57. 1980, New York: Wiley.

17. Leung, W.P. and A.C. Tam, *Noncontact monitoring of laser ablation using a miniature piezoelectric probe to detect photoacoustic pulses in air*. Applied Physics Letters, 1992. **60**(23): p. 23-25.
18. Bregar, V.B. and J. Možina, *Optoacoustic analysis of the laser-cleaning process*. Applied Surface Science, 2002. **185**(3): p. 277-288.
19. Diaci, J. and J. Možina, *Multiple-pass laser beam deflection probe for detection of acoustic and weak shock waves in fluids*. Review of Scientific Instruments, 1995. **66**(9): p. 4644-4648.
20. Jankowska, M. and G. Śliwiński, *Acoustic monitoring for the laser cleaning of sandstone*. Journal of Cultural Heritage, 2003. **4**: p. 65-71.
21. Gómez, C., et al., *Comparative study between IR and UV laser radiation applied to the removal of graffiti on urban buildings*. Applied Surface Science, 2006. **252**(8): p. 2782-2793.
22. Angel Eduardo Villarreal-Villela, L.P.C., *Monitoring the Laser Ablation Process of Paint Layers by PILA Technique*. Open Journal of Applied Sciences, 2016. **6**(9): p. 626-635.
23. Tserevelakis, G.J., et al., *On-line photoacoustic monitoring of laser cleaning on stone: Evaluation of cleaning effectiveness and detection of potential damage to the substrate*. Journal of Cultural Heritage, 2018.
24. Skoulikidis, T., D. Charalambous, and P. Papakonstantinou-Ziotis, *Mechanism of Sulphation by Atmospheric SO₂ of the Limestone and Marble of Ancient Monuments and Statues: III. Further proofs of the validity of the galvanic cell model*. British Corrosion Journal, 1983. **18**(4): p. 200-202.
25. Vergès-Belmin, V. and C. Dignard, *Laser yellowing: myth or reality?* Journal of Cultural Heritage, 2003. **4**: p. 238-244.
26. Pouli, P., et al., *The laser-induced discoloration of stonework; a comparative study on its origins and remedies*. Spectrochim Acta A Mol Biomol Spectrosc, 2008. **71**(3): p. 932-45.
27. Papanikolaou A., S.P., Philippidis A., Melessanaki K., Pouli P. *Towards the understanding of the two wavelength laser cleaning in avoiding yellowing on stonework: a micro-Raman and LIBS study*. in *Lasers in the Conservation of Artworks XI, Proceedings of the International Conference LACONA XI*. 20–23 September 2016. Kraków, Poland: NCU Press, Toruń 2017.
28. Potgieter-Vermaak, S.S., et al., *Micro-structural characterization of black crust and laser cleaning of building stones by micro-Raman and SEM techniques*. Spectrochimica Acta Part A: Molecular and Biomolecular Spectroscopy, 2005. **61**(11): p. 2460-2467.
29. M Gavino, B.H., M Castillejo, M Oujja, E Rebollar, V Vergès-Belmin, W Nowik, C Saiz-Jimenez, *Black crusts removal: the effect of stone yellowing and cleaning strategies*. Air Pollution and Cultural Heritage. London: AA Balkema, 2004: p. 239-245.
30. Zafiropulos, V., et al. *Synchronous Use of IR and UV Laser Pulses in the Removal of Encrustation: Mechanistic Aspects, Discoloration Phenomena and Benefits*. in *Lasers in the Conservation of Artworks*. 2005. Berlin, Heidelberg: Springer Berlin Heidelberg.
31. Frantzikinaki, K., et al. *The Cleaning of the Parthenon West Frieze by Means of Combined IR- and UV-Radiation*. in *Lasers in the Conservation of Artworks*. 2007. Berlin, Heidelberg: Springer Berlin Heidelberg.

32. Garrison, B.J. and R. Srinivasan, *Laser ablation of organic polymers: Microscopic models for photochemical and thermal processes*. Journal of Applied Physics, 1985. **57**(8): p. 2909-2914.
33. Watkins, K.G., C. Curran, and J.-M. Lee, *Two new mechanisms for laser cleaning using Nd:YAG sources*. Journal of Cultural Heritage, 2003. **4**: p. 59-64.
34. Carslaw, H. and J. Jaeger, *Conduction of Heat in Solids*. 1959, London: Oxford University Press.
35. Salimbeni, R., R. Pini, and S. Siano, *A variable pulse width Nd:YAG laser for conservation*. Journal of Cultural Heritage, 2003. **4**: p. 72-76.
36. Paltauf, G. and P.E. Dyer, *Photomechanical Processes and Effects in Ablation*. Chemical Reviews, 2003. **103**(2): p. 487-518.
37. Wang, L.V., *Tutorial on Photoacoustic Microscopy and Computed Tomography*. IEEE Journal of Selected Topics in Quantum Electronics, 2008. **14**(1): p. 171-179.
38. Simandoux, O., et al., *Influence of nanoscale temperature rises on photoacoustic generation: Discrimination between optical absorbers based on thermal nonlinearity at high frequency*. Photoacoustics, 2015. **3**(1): p. 20-25.
39. Calasso, I.G., W. Craig, and G.J. Diebold, *Photoacoustic Point Source*. Physical Review Letters, 2001. **86**(16): p. 3550-3553.
40. Liu, J.M., *Simple technique for measurements of pulsed Gaussian-beam spot sizes*. Optics Letters, 1982. **7**(5): p. 196-198.
41. M.A. Founti, et al., *Inducing energy storage properties in white dolomitic marble tiles - Industrial tests and property evaluation*. Global Stone Congress, 2010: p. 6.
42. Waples, D.W. and J.S. Waples, *A Review and Evaluation of Specific Heat Capacities of Rocks, Minerals, and Subsurface Fluids. Part 1: Minerals and Nonporous Rocks*. Natural Resources Research, 2004. **13**(2): p. 97-122.
43. V. Shushakova, et al., *Marble decay induced by thermal strains: simulations and experiments*. Environ Earth Sciences, 2013. **69**(4): p. 17.
44. Bangham, D.H. and R.E. Franklin, *Thermal expansion of coals and carbonised coals*. Transactions of the Faraday Society, 1946. **42**(0): p. B289-B294.
45. Schofield Paul, F., S. Knight Kevin, and C. Stretton Iona, *Thermal expansion of gypsum investigated by neutron powder diffraction*, in *American Mineralogist*. 1996. p. 847.